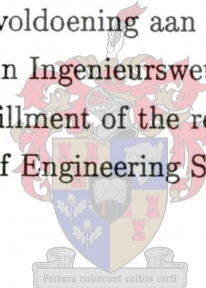


# The Automated Detection and Analysis of Gravitational Microlensing Events

Ruby van Rooyen

Tesis ingelewer ter gedeeltelike voldoening aan die vereistes vir die graad van  
Magister in Ingenieurswetenskap.

Thesis presented in partial fulfillment of the requirements for the degree of  
Master of Engineering Science.



Supervisors: Prof. B.M. Herbst - University of Stellenbosch  
Dr. J. Menzies - South African Astronomical Observatory  
Prof. D. Weber - University of Stellenbosch

December 2000

Verklaring:

Ek, die ondergetekende, verklaar hiermee dat die werk in hierdie tesis vervat, my eie oorspronklike werk is en dat ek dit nie vantevore in die geheel of gedeeltelik by enige universiteit ter verkryging van 'n graad voorgelê het nie.

Declaration

I the undersigned, hereby declare that the work contained in this thesis is my own original work and that I have not previously in its entirety or in part submitted it at any university for a degree.

## Abstrak

Hierdie tesis beskryf tegnieke om die identifikasie, prosessering en analise van gravitasie mikro-lens gebeure te outomatiseer. Die analise van hierdie gebeure is belangrik aangesien dit gebruik word vir die opsporing van planete buite ons sonnestelsel. Om gebruik te maak van 'n reeks beelde wat een van hierdie gebeure vertoon moet ons die volgende probleme aanspreek: beeld registrasie, verwydering van die agtergrond en die modulering van die verspreiding van die lig van 'n puntbron deur die atmosfeer.

Ons verkry *registrasie* deur die berekening van die snypunte van sirkels met middelpunte by sekere voorwerpe op die beeld. Na registrasie kan ons die invloed van die *agtergrond* bepaal deur gebruik te maak van die waterskeidingsalgoritme. Dit stel ons in staat om die relatiewe helderheid van die voorwerpe ondersoek deur die voorwerpe te isoleer en te sommer oor die area van 'n voorwerp. 'n Grafiese voorstelling van die helderhede dui vir ons die relatiewe variasies in die helderhede van die mikrolens objek tussen die beelde aan. Ons ondersoek die vorm van die kromme asook die moontlike voorkoms van 'n 'blik' deur middel van *wavelet* analiese en die *LOESS* metode.

Die vorm van die kromme word gebruik vir die identifikasie en klassifikasie van die verskillende mikro-lens gebeure en kan uitgebrei word om ook veranderlike sterre te ondersoek. Die teenwoordigheid van 'n 'blik' op die data wys op die moontlik teenwoordigheid van 'n planeet naby aan die bron wat ons ondersoek.

## Abstract

In this thesis we addressed some issues concerning the automation of the detection, processing and the analysis of gravitational microlensing events, which are currently being used in the search for extra-solar planets.

We were provided with a series of data images containing a microlensing event. Using these images we address several practical problems: registration, background subtraction and some PSF modelling.

*Registration* is accomplished by using the intersection points of circular arcs drawn around stellar objects. After which the influence of the sky *background* is removed by using the watershedding algorithm and plane fitting.

Our analysis is based on *relative* brightness — to counter seeing, the brightness of stars are calculated by isolating the objects from the background and summing over the area. A brightness variation curve is plotted and the trend of the lensing event and the position of a blip are extracted using *wavelets*, calculating general trends and *LOESS*.

The trend of the brightness variation curve can be used for both identification and classification of various events. It can also be used for the identification and classification of variable stars. Blip analysis is used to detect the presence of a planet (or dark body) in the vicinity of the source.

# Contents

<b>1</b>	<b>Introduction</b>	<b>1</b>
<b>2</b>	<b>Background</b>	<b>5</b>
2.1	Gravitational Microlensing . . . . .	5
2.2	The Search for Dark Matter . . . . .	7
2.2.1	Scope of the Investigation . . . . .	8
2.2.2	Planets? . . . . .	9
2.3	Data Images . . . . .	9
2.3.1	Discussion of the Images Used in the Investigation . . . . .	10
2.3.2	Seeing . . . . .	11
2.3.3	Zenith Distance (Extinction) . . . . .	11
2.3.4	Background . . . . .	11
2.3.5	Noise . . . . .	12
2.3.6	Distortion Effects on the Images . . . . .	13
2.3.7	The Conversion and Displaying of the Image (.fits) Files . . . . .	14
<b>3</b>	<b>Current Techniques</b>	<b>17</b>
3.1	DoPHOT . . . . .	17
3.1.1	General Description of DoPHOT's Object Recognition . . . . .	18
3.1.2	DoPHOT: Approaches to Different Anomalies . . . . .	18
3.1.3	Point Spread Function (PSF) . . . . .	19
3.1.4	Saturated Stars . . . . .	20
3.2	Image Subtraction . . . . .	20
<b>4</b>	<b>Pre-processing of the Images</b>	<b>23</b>
4.1	Registration Through Pattern Recognition . . . . .	24
4.1.1	Problems Encountered with the Images . . . . .	24

**CONTENTS**

v

4.1.2	Registration Through Triangulation . . . . .	25
4.1.3	Registration using the Intersection Points of Circles . . . . .	27
4.1.4	Remarks . . . . .	28
4.1.5	Matching of the Images . . . . .	29
4.1.6	Accuracy of the Registration Technique . . . . .	31
4.1.7	Comparison of the Two Registration Techniques . . . . .	32
4.1.8	Possible Future Expansion . . . . .	32
4.2	Subpixel Registration using Interpolation . . . . .	33
4.2.1	Basic Description and Approach . . . . .	33
4.3	Sky Background Determination and Removal . . . . .	34
4.3.1	Discussion of the Method . . . . .	34
4.4	Watershedding . . . . .	37
4.5	Point Spread Function (PSF) Modelling . . . . .	41
4.6	Normal Density Distribution Function . . . . .	42
<b>5</b>	<b>Data Extraction and Analysis</b>	<b>46</b>
5.1	Wavelets . . . . .	46
5.2	General Trend . . . . .	50
5.3	(Robust) Locally Weighted Regression (LOESS) . . . . .	51
<b>6</b>	<b>Data Analysis and Results</b>	<b>53</b>
6.1	Intensity Variations . . . . .	54
6.2	Methods of Analysis . . . . .	56
6.2.1	Data Subtraction . . . . .	56
6.2.2	Wavelets . . . . .	58
6.2.3	General Trend . . . . .	61
6.3	Finding a Blip . . . . .	62
6.3.1	Data Subtraction . . . . .	63
6.3.2	Wavelets . . . . .	64
6.3.3	General Trend . . . . .	67
6.4	Locally Weighted Regression (LOESS) . . . . .	68
<b>7</b>	<b>Conclusion</b>	<b>71</b>
	<b>Appendix A: Data Images</b>	<b>76</b>

<i>CONTENTS</i>	vi
<b>Appendix B: Seeing</b>	<b>79</b>
<b>Appendix C: Poisson Statistics</b>	<b>81</b>

# List of Figures

2.1	A graphical illustration of the mechanism of gravitational microlensing. . .	6
2.2	A model of what the observed lightcurve for a planetary system with 8 planets might look like. . . . .	9
2.3	Atmospheric Extinction . . . . .	12
2.4	The peak brightness of a star varies from image to image. . . . .	13
2.5(a):	Display of a sky-image using histogram equalization. . . . .	16
2.5(b):	Display of a sky-image using warp. . . . .	16
4.1(a):	The reference image. . . . .	24
4.1(b):	The comparison image. . . . .	24
4.2	Illustration of the basic concept of the triangulation method. . . . .	26
4.3	Graphical representation of the method of circle intersection. . . . .	28
4.4	The reference image . . . . .	30
4.5	The comparison image. . . . .	30
4.6	The comparison image after registration. . . . .	30
4.7(a):	The difference between the reference image and the registered comparison image. . . . .	30
4.8	The relative error of each image against the respective distances of translation. . . . .	31
4.9	The relative error of each image against the respective angles of rotation. . . . .	31
4.7(b):	The differences between the reference image and the registered comparison image. . . . .	34
4.10(a):	A histogram of the brightness values. . . . .	35



## LIST OF FIGURES

viii

4.10(b): The lower grayscale values show the definite maximum that exist there.	35
4.10(c): The quadratic spline fitted over the maximum formed in the lower grayscale. . . . .	35
4.11 A cubic smoothing spline is fitted through these points as indicated by the solid line. . . . .	36
4.12 The plane, approximating the background. . . . .	37
4.13(a): Enlargement of part of the image to show the lensing event area. . . . .	38
4.13(b): Image with the watersheds superimposed on it. . . . .	38
4.14 The histogram shows the maximum amount of pixels to be at the lowest values. . . . .	39
4.15 Plane fitted over the image using the background determined around isolated stars. . . . .	39
4.16 Plane fitted over the images using the background determined through use of the watersheds. . . . .	39
4.17 A mesh from one of the isolated stars that was used to determine the back- ground plane. . . . .	42
4.18 A contour plot of the same star used in the mesh of the previous figure. . .	42
4.19 A normal distribution in two dimensions. . . . .	43
4.20 The reference image that needs to be softened. . . . .	44
4.21 The comparison image that we want to simulate by softening the reference image. . . . .	44
4.22 The reference image after softening by application of the Gaussian filter. .	45
6.1 Two images showing the increase in the intensity of the lensing object. . .	54
6.2 The three signals represent the change in the brightness values of three objects over a period of 50 days. . . . .	55
6.3 The subtraction of the data points of each signal. . . . .	57
6.4 Complete set of data points after smoothing with wavelet analysis. . . . .	59
6.5 If we subtract the averages of the data, as determined using the wavelets, from a general trend. . . . .	59

<i>LIST OF FIGURES</i>	ix
6.6 Graph showing the behaviour of the detail coefficients. . . . .	60
6.7 The increasing (red) curve shows the residual after the lensing signal was subtracted from the general trend. The two curves (blue) situated around zero are the reference signals subtracted from the general trend. . . . .	61
6.8 Three signals representing the data to analyse. . . . .	62
6.9 Data signals of the data set with the artificial blip, with the blip clearly visible and a slight indication of a trend. . . . .	63
6.10 Decomposition and detail of the lensing data using the wavelet toolbox graphics display. . . . .	65
6.11 The top (red) graph shows the residual after the subtraction of the detail coefficients of the two reference signals. The bottom two graphs (blue) show the residual after subtracting the respective reference detail coefficients from the lensing detail coefficients. . . . .	66
6.12 The top (red) graph shows the wavelet detail of the data containing the artificial blip. The bottom (yellow) graphs shows the differences after the data points of the same data have been subtracted. . . . .	66
6.13 Using the data with the artificial blip. . . . .	67
6.14 LOESS fit through the lensing data containing the artificial blip, using a linear polynomial and $f = 0.3$ . . . . .	69
6.15 LOESS fit through the data of the first reference star, using a linear polynomial and $f = 0.9$ . . . . .	69
6.16 LOESS fit through the data of the second reference star, using a linear polynomial and $f = 0.9$ . . . . .	70
1 Illustration of the wavefront distortions of the light as it passes through the atmosphere. . . . .	80
2 A typical Poisson density distribution function. . . . .	83

**Acknowledgements:**

The author wishes to thank:

The PLANET collaboration for providing the images investigated in this thesis,  
the South African Astronomical Observatory for the use of their facilities,  
astronomers J. Menzies, C. Koen and D. O'Donoghue for their time, patience and sharing  
their knowledge.

# Chapter 1

## Introduction

Astronomers need to examine vast quantities of digital images. Often what they are looking for are subtle changes in the absolute brightness of an object, or to identify objects that suddenly become visible. A particularly important topic at the moment is the search for extra-solar planets. Since these planets are invisible themselves and the most interesting ones revolving around small stars of about the size of the sun, it is impossible to detect them directly and one has to resort to indirect evidence. One of the techniques currently under investigation is the analysis of so-called microlensing events. This happens when a low-mass object passes between us, the observers, and the distant object of interest. The gravitational forces of the low-mass object acts as a gravitational 'lens', bending light that will normally pass the observer towards him, causing an increase in brightness. If it so happens that the distant object have planets near it, their presence should be indicated by very specific variations in its brightness.

The scientific problem we are interested in, is two-fold. In the first place there is the problem of detecting an event among a mass of CCD images. In the second place, we are interested in analysing the event in order to detect any variations due to the presence of planets. Note that events are found by collaborations and once detected, they are continuously observed throughout their duration. One such collaboration (PLANET) has provided us with a series of 30 images, containing a microlensing event, for investigation.

The automatic detection and analysis of an event is not an easy one and the main culprit is the atmosphere. Every time a telescope is pointed to the sky, the seeing<sup>1</sup> is different. This means that the maximum brightness of the stars is different and often a dim object

---

<sup>1</sup>The term 'seeing' is defined in detail in appendix B page 79

may not even be visible at all. It is not even straightforward to measure the apparent brightness of an object on a CCD. Because of fluctuations in the atmosphere the light from a distant point source is scattered over a finite extent, the so-called Point Spread Function (PSF), with the boundaries merging with the background. This problem is particularly severe in crowded regions of the sky where the boundaries between different objects become indistinct. There is also the technical matter of registering the images. Although telescope guiders allow telescopes to be aligned with a specific object, this is never exact. Thus in practice one finds that although two images may be of the same region of the sky, they are never exactly aligned, and may even differ to a considerable extent. The technical problem is therefore to match corresponding objects in the different images, allowing one to align the images. There is also the nontrivial problem of CCD limitations. For instance, during long exposures of bright objects the CCD may become saturated which basically means that it is unable to capture the full magnitude of the brightness. This amounts to an irrecoverable loss of information.

Different approaches to the problem have been explored. Systems like DoPHOT [Schechter et. al. 1993] model the background influence and noise, and then subtract it from the image along with any saturated stars. Another analysis toolbox is IRAF, which is a package of image analysis tools, one of which is a program called DAOPHOT which has a similar approach, though not identical, to that of DoPHOT. The effects of seeing on an object are approximated through PSF modelling. To analyse the brightness variation of objects, image subtraction [Alard 1997] is used. By subtracting the images from each other, the differences remaining gives a clear indication of the behaviour of the brightness of an object through the series.

In our case the lensing event is located in a sparsely populated region of the sky. All the objects we are concerned with are isolated; we assumed this in developing our methods in which case there is no need to develop methods for crowded fields. Some of the suggested techniques can be used or easily adapted for application to crowded fields, while others need to be refined. These methods might be used in conjunction with the standard techniques, often leading to more efficient results after analysis.

First we address the pre-processing of the images. The registration of the images amounts to the elimination of the rotation and translation differences between the non-aligned images. After this the removal of the background follows to get rid of any radiation that does not originate from the objects. We end with a mention on the modelling of the effect that the atmosphere has on the light from the source (PSF). We aim to suggest a variety of

alternative methods that includes registration using the intersection points of circular arcs and the watershed algorithm used in determining the background of the images.

The detection and analysis of an event depends on the way that the brightness of the object changes over time. The brightness of the objects is determined by isolating them from the images. For this we determine the best position to consider as an edge between the object and the background, remove the background influence and sum over the area. All the analysis is done using techniques such as wavelet analysis and locally weighted regression.

All the development and implementation is done using the MATLAB package.

Structure of the thesis: Chapter 2 gives an introduction to the astronomical terms and concepts used in the rest of the document, along with short discussions explaining the interpretation and some basic problems of the covers the basic astronomical background and descriptions of the astronomical images used. Chapter 3 consists of summaries describing the techniques that are currently being used in astronomy (at SAAO) for the pre-processing and analysis of the images. These include the registration and background removal techniques. Chapter 4 contains a short description of our suggested methods for pre-processing the images and the results achieved during the implementation of these techniques. Chapter 5 provides background covering the methods suggested for the analysis of the data with an emphasis on the wavelet and LOESS techniques. Chapter 6 shows the actual analysis and the results of these methods. These results are non-conclusive, because the training and testing sets consist basically of the same images, but we are able to show the efficiency of wavelet analysis as well as some results obtained after applying the LOESS technique. Chapter 7 presents our conclusions.

Most of the astronomical definitions were taken from the Astronomical Dictionary [Ridpath 1997] and the mathematical definitions from the Mathematical Dictionary [Borowski et. al. 1989].

Summary of acronyms used in the discussion:

**ADU** Analog to Digital Unit

**CCD** Charge Coupled Device

**FITS** Flexible Image Transport System

**IRAF** Image Reduction and Analysis Facility

**LOESS** Locally Weighted Regression

*CHAPTER 1. INTRODUCTION*

4

**PLANET** Probing Lensing Anomalies **NET**work

**PSF** Point Spread Function

**SAAO** South African Astronomical Observatory

## Chapter 2

# Background and Definitions

### 2.1 Gravitational Microlensing

Gravitational lensing is the bending of light caused by the gravity of an object lying between the light source and the observer [Paczynski 1996]. When a point object lies in the line of sight to a distant point source, the gravity of this point object has an effect on the path of the light originating from the source. This gravitational bending of the light from the source causes the brightness of the object to vary in a very specific way accompanied with the formation of two additional images. This variation in brightness is caused by the fact that light from the source that would normally pass the observer now gets deflected towards the observer.

Our applications are developed for microlensing events. The difference between gravitational lensing and gravitational microlensing is mainly a scaling problem. For gravitational lenses the mass of the lensing object is approximately the same as a galactic mass and the separation between the images is approximately one arcsecond. For gravitational microlenses the mass of the lensing object is approximately the same as a stellar mass and the image separation is only approximately  $10^{-3}$  arcseconds. Thus it is not possible to see the individual images with the current resolutions provided with available instrumentation. These sources (stars) are expected to vary in brightness in a characteristic manner if low-mass stars or planets pass in front of them.

In our case, the source will be located in the Galactic Bulge — the roughly spherical distribution of stars that forms the central hub of the Galaxy — with the lensing object located somewhere between the Bulge and us.



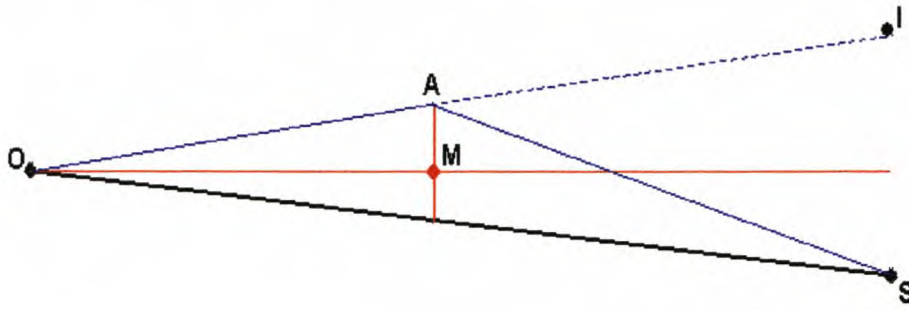


Figure 2.1: A graphical illustration of the mechanism of gravitational microlensing. The observer, lensing mass and the source are located at points  $O$ ,  $M$ ,  $S$ , and  $\alpha$  is the angle with which the lightray from the source is deflected by the point mass.  $D_d$  and  $D_s$  is the distances from the observer to the lens and to the source.  $D_m$  is the distance from the lens to the source,  $SO$  is the path of a lightray if the lensing mass  $M$  is absent,  $SAO$  is another lightray that is deflected by the gravitational influence of the lensing mass  $M$ .  $I$  is the position at which a distorted image of the object will appear.

For more information see the comprehensive overview of the theory of gravitational microlensing by [Paczynski 1996]. This is also the article from which we extracted the graphical illustration (figure 2.1).

Let us consider the simple case where we have a single point mass  $M$  deflecting the light from a single point source  $S$ , as illustrated in figure 2.1. A lightray (bottom lightray) emitted from the source  $S$  will reach the observer along the bottom line  $\bar{OS}$  in the absence of the deflecting lens mass  $M$ . If we insert the lensing mass  $M$  between the observer and the source and we consider another lightray (top, blue lightray) emitted from the source  $S$ . The gravity of the lensing mass  $M$  interacts with this lightray at point  $A$  and bends the lightray in the direction of the observer  $O$ . Thus the lightray travelled along the path  $SAO$ . The observer does not observe that the lightray travelled along this path, but sees an image of the object at  $I$  (on a straight line) instead of the object at  $S$ . The same will happen with some other lightrays in the same plane and this causes the formation of two images around the source. When the formation of these images are so close to the source that only a variation in brightness is observed, it is a microlensing event.

## CHAPTER 2. BACKGROUND

**2.2 The Search for Dark Matter**

A few years ago astronomers became interested in the search for extra-solar planets. To be called a planet, an object must be as massive or more massive than Pluto and less massive than ten times the mass of Jupiter ( $< 0.01$  solar masses). Unlike stars, planets do not produce light of their own but merely reflect the light of the star(s) they orbit. Planets are one manifestation of so-called dark matter, whose nature is unknown except for their gravitational effects and the fact that they emit no radiation [Ridpath 1997]. Thus the presence of such dark material can only be inferred from its gravitational effects on the motions of stars and galaxies [Marcy et. al. 1998]. One of the proposed methods for finding planets is with the technique of gravitational microlensing. This is done by assuming that stars should vary in brightness in a characteristic manner if planets pass in front of them [Sackett 1999].

The main problem with the observation of planetary disturbances on microlensing lightcurves is the fact that these disturbances happen very fast and a number of observations — over any event that might happen — are necessary. The important aspect of the event is the timescale; that is the time it takes the object to cross the angular Einstein ring radius. The Einstein ring  $\Theta_E$  is a function of the mass of the lens  $M_{lens}$ , the distance between the observer and the source  $D_s$ , the distance between the observer and the lens  $D_d$  and the distance between the lens and the source  $D_m$ :

$$\Theta_E = \left( \frac{4GM_{lens}}{c^2} \cdot \frac{D_m}{D_s D_d} \right)^{\frac{1}{2}} . \quad (2.1)$$

With the timescale given by the time it takes the source to move with respect to the lens by one Einstein ring radius:

$$timescale = t_E = \frac{D_s \Theta_E}{v} . \quad (2.2)$$

Here  $v$  is the relative velocity of the source with respect to the lens.

Consider a number of sources at approximately the same distance from the observer (so  $D_s$  is approximately the same for all the sources). Also assume that light from the sources are affected by lenses at approximately the same distance  $D_d$  from the observer and all of them have approximately the same proper motion. Thus the only free parameter in the equation (2.2) (the timescale equation) is the mass of the lens  $M_{lens}$ , and from equation (2.1) we find that the timescale  $t_E$  is proportional to the square root of the mass of the lens ( $M_{lens}$ ):

$$t_E \propto M_{lens}^{\frac{1}{2}} . \quad (2.3)$$

Typically we find this timescale to be in the order of 20 to 50 days for sources in the Bulge. For example, consider a single source situated approximately in the Bulge and a single low-mass lensing object at approximately half of that distance. If there is a planet associated with the source, we also find

$$t_{E,planet} \propto M_{planet}^{\frac{1}{2}} . \quad (2.4)$$

The relative timescale for a planetary perturbation of say the same mass as Jupiter is

$$\frac{t_{E,planet}}{t_E} \propto \left( \frac{M_{planet}}{M_{lens}} \right)^{\frac{1}{2}} \simeq (10^{-3})^{\frac{1}{2}} . \quad (2.5)$$

Thus the timescale is on the order of a few hours to a few days, leading to the necessity of frequent (hourly) observations for the detection of these events. These factors lead to the formation of collaborations between astronomical observatories. One such collaboration is the **Probing Lensing Anomalies NETwork** (PLANET); see the PLANET webpage, available at [www.astro.rug.nl/~planet](http://www.astro.rug.nl/~planet). Due to the locations of the members of this collaboration in the Southern Hemisphere, the result is that around the clock observations are possible. The only interruptions are caused by bad weather, leaving gaps in the data.

### 2.2.1 Scope of the Investigation

We will focus our investigation primarily on the following issues:

1. Automate the detection of a lensing event from a sequence of images.
2. Given the position (co-ordinates) of the lensing event on at least one of the images: Analyse the light-curve, which represents the changes (and the pattern of these changes) in the brightness of the source object with time.

In practice the lensing events are found by surveys from several collaborations worldwide. However, it will be useful if the same detection technique can be applied to other phenomena such as variable stars. Although this issue was not investigated in as much detail as the trend are — mainly owing to a lack of data — we show that our approach is capable of addressing this issue as well.

In addition: There exists a large archive of detailed images for a series of sky-fields. It is obvious that a lot of useful data is just being ignored, since the known lensing event is the only object really investigated on these images. It is therefore natural to try to use as much as possible of the available data.

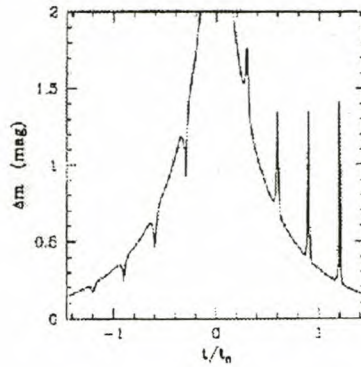


Figure 2.2: A model of what the observed lightcurve for a planetary system with 8 planets might look like.

### 2.2.2 Planets?

Since we can only observe intensity variations we have no direct information about the size, mass or distance of the source. What we do know is that very short lensing events are due to lenses that are either very close to the source or very close to the observer. On the other hand, lenses that move almost along the line of sight causes very long events [Paczynski 1996]. For sources in the Galactic bulge and lensing objects that are situated nearer to us, the relative motions are more or less the same for all the objects. Thus the timescale for a planetary event is usually very short.

When considering an event where planets or a planetary system is involved, we are moving into the domain of multiple lenses, which is not discussed here. It suffices to say that if there is a planet associated with the source, this will produce a spike (or dip) on the otherwise smooth lightcurve of the lensing event and this disturbance is expected to be of short duration. Such local anomalies are illustrated in figure 2.2, which shows a model light-curve of a planetary system.

## 2.3 Data Images

The data images used in the investigation are all in the FITS-standard format [NASA 1990]. FITS is an acronym for the name **F**lexible **I**mage **T**ransport **S**ystem. The flexible image transport systems' development was necessitated by the need for a standard format for the transferring of astronomical data from one installation to another.

This format type is specific to astronomical images and is not a known format to most common converters and applications. Since it was developed for international use, the format is well documented and the specifications are readily available.

### 2.3.1 Discussion of the Images Used in the Investigation

We will give a short discussion of the images themselves and their behaviour and properties. The images that are used in this application are the data images acquired by the 1.0m telescope at Sutherland, using a Charge Coupled Device (CCD) detector [Gullixson 1992]. A CCD is essentially a very high sensitivity, high-resolution version of the light sensitive element in video cameras. Some effects in the raw images, caused by instrumentation and software were corrected and need not concern us.

To study these images using the available mathematical tools some adaptation to the handling of file input was necessary. Flexible Image Transport System (FITS) files consists of an ASCII header and a binary block which contains the image (for more information see appendix A page 76). These images are exposures taken of a microlensing event and the surrounding sky.

Our efforts are aimed at making some suggestions toward the automation of the comparison of the images in a sequence and to try to extract the brightness variation of the lensing object.

For the automated analysis of the brightness variations of an object over a series of images, the two images that are being compared at any one time must be as similar as possible without over-processing the images. Thus some pre-processing of at least one of the two images is required. To accomplish this matching, we need to consider some basic properties of the images.

The images, taken with the same detector and from the same site, showed differences in the stellar object structure from one image in the series to another.

All the factors affecting the image quality will be addressed individually during the discussions, since it is necessary to consider all these effects if one wishes to analyse the evolution of a gravitational microlensing event through a series of data images.

Some factors that play a major role in the quality of these images are the seeing conditions when the image was taken, the zenith distance (extinction), the sky background and the noise on the image.

### 2.3.2 Seeing

Seeing is a problem that is caused by the existence of a turbulent atmosphere (see appendix B on page 79) with consequent fluctuations of path length. What this means is that the light from a point source, the stellar object, is scattered by the atmosphere in a localised area [Masson 1993]. This gives rise to a blurred representation of the object on the image during a long exposure. If very short exposures are taken they produce a speckle pattern [Cornwell 1987]. An exposure time of approximately 0.1 seconds is required for the speckle pattern to change significantly.

### 2.3.3 Zenith Distance (Extinction)

Atmospheric extinction depends on the zenith distance, which is the angle between the zenith and the position of the object being observed. Atmospheric extinction is the dimming of starlight by the terrestrial atmosphere. The longer the path length that the starlight traverses through the atmosphere, the more it is dimmed. In other words, a star close to the horizon (figure 2.3) will be dimmed more than one close to the zenith — directly above the observer — since extinction will increase with the zenith angle ( $X = \sec z(1 - 0.0012(\sec^2 z - 1))$ ), where  $z$  is the zenith distance ([www.jach.hawaii.edu](http://www.jach.hawaii.edu)). For small angles we can assume  $X \simeq \sec z$ .

For large zenith angles the atmosphere acts like a prism that gives rise to differential refraction. This causes the predominantly blue light from blue stars to be refracted through a different angle than the predominantly red light from red stars, causing the relative positions of the stars to change.

### 2.3.4 Background

The background radiation is electromagnetic radiation that arrives at the telescope detector, which does not come from the source under observation [Ridpath 1997]. These unwanted counts must be subtracted from the observed counts coming from the source [Hopkins 1980]. Also contributing to the background is light from very dim stars hidden in the background and some stray light that is scattered by the atmosphere. The latter is mostly light from the moon and usually causes some problems when the moon is up and close to the field of observation. Crowded starfields also create specific problems. Light from the surrounding stars might overlap, making it difficult to isolate individual stars and

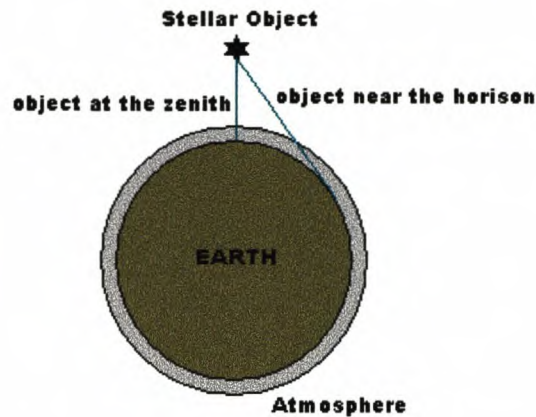


Figure 2.3: When the stellar object is situated at the zenith it is situated right above the observer and the light has to pass through the least amount of atmosphere. When the stellar object is low on the horizon, it passes through more of the atmosphere to reach the observer.

thus causing the surrounding background to be much brighter.

### 2.3.5 Noise

Background noise is all the unwanted interference effects that superimpose random fluctuations on the signal from the source. This noise has several origins, but the most significant is the photon noise in the star at brighter levels and the sky at lower levels. Another source of noise is the random movements of electrons in the receiving apparatus, called thermal noise [Ridpath 1997]. When using photon-counting devices (such as CCD detectors) there are usually Poisson statistics (see appendix C on page 81) involved. Poisson statistics arise from the way in which the source emits the photons.

For the CCD the signal to noise (S/N) is given by the ‘CCD equation’ [Howell 1989]:

$$S/N = \frac{N_*}{[N_* + n_{pix}(N_s + N_d + N_r^2)]^{\frac{1}{2}}}, \quad (2.6)$$

where

$N_*$  is the total number of photons from the source with the sky contribution subtracted.

$n_{pix}$  is the number of pixels contained within the software aperture.

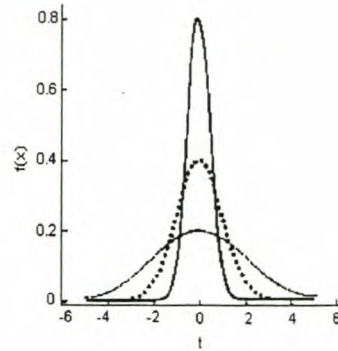


Figure 2.4: The peak brightness of a star varies from image to image with a high peak during for good seeing conditions and a lower peak for worse seeing conditions. However it still holds that  $\int I_1 = \int I_2 = \int I_3$ , meaning that the total intensities are still the same.

$N_s$  is the total number of sky photons per pixel.

$N_d$  is the dark current in photons per pixel.

$N_r$  is the read-out noise in electrons per pixel.

Dark current is produced in the bulk of the detector material and is reduced by cooling the detector.

Read-out noise is produced in the read-out amplifier, which converts the number of electrons into a voltage that can be digitised. Read-out noise is not usually a problem for broadband (visible) observations.

### 2.3.6 Distortion Effects on the Images

It is important that we distinguish between the intensities of the objects and the signal counts<sup>1</sup> that we get from the detector. An object on an image can be represented as shown in figure 2.4. As the seeing conditions change from one observation to another the shape of the object changes from one image to another. When the seeing is bad, the object will be spread out over a wider area and with good seeing it will be more concentrated. What we find is that the total areas underneath the curves, which is related to the absolute brightness of the object, are approximately equal. Thus the maximum recorded intensity on the detector changes from one image to another.

<sup>1</sup>The signal count is related to the number of photons that is observed for that object



Since the apparent brightness on the detector is translated into a grayscale<sup>2</sup> image, the peak brightness recorded on the detector determines the maximum grayscale of an image. Typically these maximum values will lie between 40 000 and 60 000 counts.

The relationship of the grayscales between two images is non-linear and since it is not possible to determine the absolute brightness of an object from the image on the detector, rescaling of an image grayscale could lead to a loss of some brightness variations.

Other problems are that although images are taken of the same region of sky, the images do not always contain exactly the same sky area. We find that stars along the edges tend to appear and disappear in various images. In most cases we observe shift, rotation and scaling differences.

### 2.3.7 The Conversion and Displaying of the Image (.fits) Files

As described in the appendices (see Appendix B on page 79), we know the format of the files and their possible distortions, and we would like to use and analyse the data from these images. For this reason we will insert a short description of the conversion of the binary image array to a MATLAB matrix. Though this is not part of the discussion on the available techniques, it forms a unit with the above discussions and is thus best presented here.

To process the astronomical sky-images the MATLAB package was used. The MATLAB converter is restricted to standard .fits files, with data in floating point format. The data is read into a matrix as an index image and has dimensions as specified in the header.

When viewing an astronomical image the greatest part of the image will be black (or near black) with a few white stars dotted around. It is impossible to see any detail in these images and astronomers usually view the images with their colourmaps inverted. Producing a negative image showing the stars as black dots on a white background. This is not only more natural to look at, but also allow some of the dimmer stars to be more readily visible. Although this is already quite an improvement it is sometimes necessary to use various methods to enhance or reduce the contrast of the image to show some 'hidden' detail during display. All the images are displayed as 16-bit images.

---

<sup>2</sup>When the CCD is read out, a number between 1 and 65 535 Analog to Digital Unit (ADU) is assigned to each pixel [ASP conf. ser. 1992]. The term grayscale is just another way of referring to these assigned values, as they exist in the sky-image matrix.

1. **Warp:** This function displays an indexed image as a texture map on a simple rectangular surface.
2. **Square root:** The square root of each element in the matrix is taken. This will reduce the values in the matrix, causing the amount of grayscales to reduce. This will help to bring out the dimmer objects that resides in the lower grayscales. This can be explained by the fact that taking the square root has a more pronounced effect on larger values than on the smaller ones. This in turn causes the grayscale values to move closer together. Thus allowing faint objects to become visible.
3. **Log:** For the same reason as mentioned above, the log of each of the elements in the matrix is taken before the image is displayed.
4. **Linear:** This function displays the image using the grayscales in the matrix as is. Except it shows the inverted image, black stars on a white background. This makes it easier to see more detail in the images.
5. **Histogram equalisation:** This function is used to enhance the contrast and to bring more detail out of the image in the display process [Gonzales et. al. 1993].

We show one of the stellar images using the methods of histogram equalisation and warping.

In figure 2.5(a) the extended structure of the stellar objects can clearly be seen. Especially with the brighter objects this poses a problem. On the image we can see the effects of crowding and seeing where multiple objects bloom over their boundaries to form one big indistinguishable object (o). When viewing this image using the warp display technique (figure 2.5(b)), a bright centre image and two dim images can be seen.

Saturation is a physical effect when a star is so bright that, during the integration time, the signal produced in a pixel exceeds some upper limit set by the electronics. Consequently the profile of the star is cut off and forms a large plateau at the maximum intensity [Schechter et. al. 1993]. All the information about the photons collected in a saturated pixel is lost. It will take extensive investigation and modelling to extract some (if any) data from a saturated object.

In figure 2.5(a) the bright sky background is also clearly visible.

Since all the information for the data image is contained in the ASCII header, it might be useful to re-examine the way in which this header is created. In the header the position of

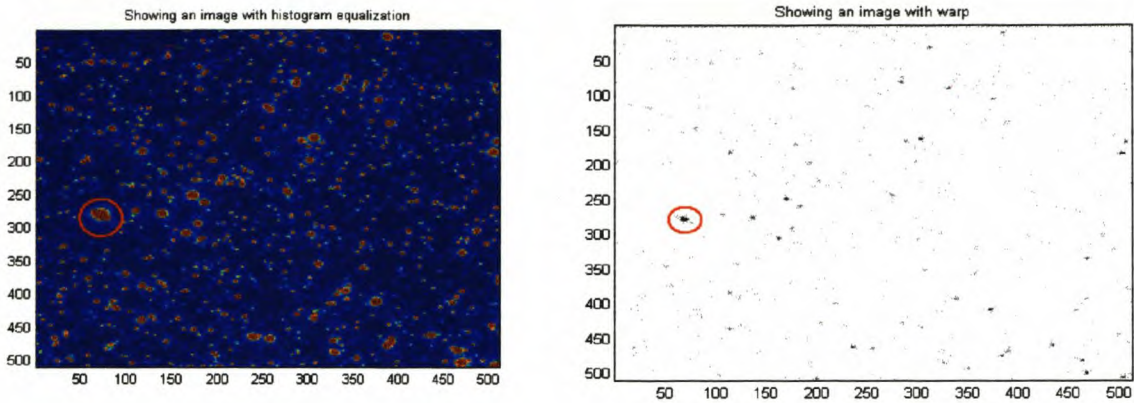


Figure 2.5(a): Display of a sky-image using histogram equalisation as an enhancement technique. The colours are the default Mat-

Figure 2.5(b): The same image displayed as a texture map shows the three objects slightly separated.

lab colourmap for displaying images after histogram equalisation. The red indicates the higher grayscales moving down to the blue for the lower grayscales. The red circle indicates a saturated object.

the field is provided (the RA<sup>3</sup> and DEC<sup>4</sup>). These are the co-ordinates to which the telescope is set for observation. If the header is also documented with the actual rest position of the telescope during an observation run, it will be easy to detect misidentification of the field directly from looking at the header information. The difference in position between the telescope and the co-ordinates of the observed field can also be used to help build a model to aid the registration of the sky-images.

<sup>3</sup>Right Ascension: The equivalent of longitude on Earth.

<sup>4</sup>Declination: The equivalent of latitude on Earth.

## Chapter 3

# Overview of Current Techniques Used for Pre-processing and Analysis

As a run-up to our techniques developed for the analysis of the microlensing events, we first present the reader with a short discussion on the currently available techniques.

There exist a variety of packages developed for the pre-processing and analysis of images. One of these packages employed at South African Astronomical Observatory (SAAO) for the reduction of PLANET data is DoPHOT [Mateo et. al. 1993]. Another program used is Image Reduction and Analysis Facility (IRAF)<sup>1</sup>, which is a collection of astronomical tools. A third method recently developed is generally known as image subtraction [Alard 1997].

### 3.1 DoPHOT

DoPHOT [Mateo et. al. 1993] is an astronomical computer package that was designed to identify 'objects' on a digital image. It can determine the positions, intensities and crude classifications of these objects. This program was written to create an automated means of image analysis with an emphasis on speedy processing.

The most relevant parts of DoPHOT for our investigation, are the methods concerned with the determination of the Point Spread Function (PSF), background and object recognition.

---

<sup>1</sup>IRAF is a collection of astronomical tools. Information concerning the installation and use of IRAF is available at [iraf.noao.edu](http://iraf.noao.edu).

### 3.1.1 General Description of DoPHOT's Object Recognition

The basic idea of DoPHOT is to use simple models to try to identify the 'objects' on a digital image [Schechter et. al. 1993]. Basic models are:

1. A Gaussian model for stars and galaxies.
2. A composition of the models of two single stars to form a model for a double star.
3. A model of a single, high pixel indicating a cosmic ray. Cosmic rays are high-energy particles travelling at nearly the speed of light and impact the earth from all directions [Hopkins 1980]. Some of the particles can also be terrestrial due to radioactivity.

Note that the Gaussian models allow for elliptical objects. Difficulties in the focus of the imager or inaccuracies in guiding<sup>2</sup> give rise to stellar objects that might be elongated to a noticeable extent in any direction (see equation (3.1)).

For cosmic rays the model is much simpler since they usually impact on a single pixel, which appears as a white dot on an image. Isolated cosmic rays can easily be identified using a delta-function as filter over the image.

The objects are then classified according to the best fitting model. The model for a single star has the dual function of also being the filter used to search for new objects. The models used in DoPHOT are described by a functions (equation (3.1) below) with seven free parameters. These parameters are the shape parameters, the object's centre, the central intensity and the background intensity. DoPHOT determines the shapes of the objects and then compare the determined shape parameters with the parameters of a 'typical' star, double star, or galaxy for identification. After an object has been identified, the appropriate fitted model is subtracted from the image. The resulting image is then searched again for progressively fainter stars, by lowering the detection threshold. Throughout this whole process DoPHOT updates a model of the noise in the image, which is used for determining whether an object is significantly above the background.

### 3.1.2 DoPHOT: Approaches to Different Anomalies

There are basically two ways of starting DoPHOT:

---

<sup>2</sup>With guiding we mean that we have selected a guide star, which we use as reference to keep the telescope trained on the object we are currently observing.

1. Using a reasonable guess for the shape parameters (this is usually the start-off mode).
2. The 'warmstart' option is when 'predetermined' objects are supplied, which are then subtracted from the image and used to compute the values for the typical shape parameters for a star. The advantage of this option is that all the measurements are made at the same relative position on all the images.

Before new objects can be searched for, it is necessary to have an approximate idea of the local sky background. In each iterative search process, DoPHOT searches for pixels with a value higher than the threshold plus the local background.

The detection of faint stars depends greatly on a good estimate of the local sky background. The pixels with high enough values are tested against the current sky model and the average value of the pixels in its neighbourhood. If both tests show a high enough signal-to-noise ratio the object is appended to the object list.

Another test is then performed on the object to determine whether it is a cosmic ray. If a significant number of pixels in the mask are saturated, that is, above a maximum threshold, a region surrounding the saturated pixels is taken out of the image.

The best fits of all the objects are then subtracted from the image. This whole iterative method works its way down the brightness levels. After the whole image has been searched for new objects, everything in the object list is fitted again to improve the classifications and the shape parameters. This means fitting the position, brightness, shape and sky values independently for each object. Since all the identified objects have been subtracted from the image, they must first be added back. After each object has been tested, it is again subtracted from the image.

At this point the model for the typical stellar PSF is updated.

The ideal is that in the final pass through the data, the fits of all the significant objects have been subtracted with only the sky background remaining.

### 3.1.3 Point Spread Function (PSF)

A goal in the design of DoPHOT was to use model fitting rather than pixel-based algorithms wherever possible. The analytical function used to represent the PSF, the surface-brightness profiles of stellar objects, is just a truncated power series for a Gaussian, as can

be seen if  $\beta_4 = \beta_6 = 1$  is substituted in equation (3.1):

$$I(x, y) = I_0 \left( 1 + z^2 + \frac{1}{2} \beta_4 (z^2)^2 + \frac{1}{6} \beta_6 (z^2)^3 \right)^{-1} + I_s \quad (3.1)$$

$$z^2 = \frac{1}{2} \left( \frac{x^2}{\sigma_x^2} + 2\sigma_{xy}xy + \frac{y^2}{\sigma_y^2} \right) \quad (3.2)$$

$$x = (x' - x_0), \quad y = (y' - y_0) \quad (3.3)$$

Usually the values are set to  $\beta_4 = \beta_6 = 1$ , but they can be changed to match the characteristics of a particular detector, telescope or combination thereof. The importance of  $\beta_4$  and  $\beta_6$  lie in the fact that they describe the slope and extension of the wings of the intensity distribution of the stellar objects. There are seven remaining free parameters in this function:

- The shape parameters:  $\sigma_x, \sigma_y, \sigma_{xy}$ ,
- the object center:  $(x_0, y_0)$ ,
- the central intensity  $I_0$ ,
- and the background intensity  $I_s$ .

Something that is not implemented in this profile-fitting model, but is nevertheless important to keep in mind, is that the profiles of bright stars are predominantly affected by the photon (Poisson) statistics (see appendix C on page 81) of the star itself. On the other hand, the profiles of faint stars are more effected by the photon statistics of the sky [Howell 1989].

### 3.1.4 Saturated Stars

DoPHOT does not attempt to fit saturated objects. It simply removes a rectangular area around the object. This can cause some confusion, since an object might be saturated on one image (and therefore removed), but not on another image, making it very difficult to cope with automating the processing and analysis of these residual images.

## 3.2 Image Subtraction

This is a newer method suggested for the analysis of the microlensing events. Only a few astronomers are currently using this technique. The person mainly responsible for the

developments of the method of analysis is C. Alard, see [Alard 1997] and [Alard 1999], who also provides the computer code.

The basic working idea is to compare two images. One image will have better seeing (the reference image) than the other (the comparison image). We use the better seeing image as reference image, but since the data on the differences is only as good as the data on the poorer comparison image, it is necessary to blur the reference image to get it as close as possible to the comparison image. This means that we need to convolve the better seeing image with some filter (or kernel) to soften (blur) or even sharpen it:

$$R(x, y) * K = I(u, v), \quad (3.4)$$

where  $R$  is the reference image,  $I$  is the comparison image and  $K$  an unknown convolution filter.

Thus we are looking for a Wiener filter [Jain 1989] which is optimal in a least squares sense, i.e., that the error in determining  $K$  is minimised.

$$\min \left[ \|I(u, v) - R(x, y) * K\|^2 \right]. \quad (3.5)$$

In general  $K$  is assumed to be a specific function, a Gaussian for example, with some free parameters that can be adjusted to minimise the residual defined above. Since a pure Gaussian may not be flexible enough to give an accurate representation [Alard 1997], the best approach would be to consider a combination of Gaussian functions as an approximation for the model of the filter (kernel). Keeping the number of add-on parameters to a minimum ensures that the model is easy to understand and implement. The general method involves a mixture Gaussian model. Usually three Gaussians are enough to represent the peak, edges and wings of each stellar object. Polynomials are then used to cut off each Gaussian since the function is defined over an infinite interval.

There is no sense in using the same filter for the whole image and indeed in his second article [Alard 1999] mentions that this filter might not be constant across the whole image. Therefore, the two options given are:

1. A dynamic model to represent the atmospheric effects
2. Breaking the image down into smaller parts and keeping the models constant for each part.

[Alard 1997] estimates the background together with the approximation of the filter (kernel) function.



The noise on the image was approximated using Poisson statistics.

After all the pre-processing of the reference image is completed, the 'conditions' of the reference image is as near to those on the comparison image as possible. The two images are subtracted leaving the essential differences between the two images.

## Chapter 4

# Pre-processing of the Images

Now that the reader is familiar with some of the existing techniques that are used, we will proceed to some of our suggested techniques. The first important issue is the fact that even if these images are taken of the same region of sky, it is impossible to get a perfect re-alignment of the telescope for each exposure. Therefore a very basic and important part of the pre-processing for these images is their registration. This re-alignment error leaves us with overlapping images of the same region of sky. With registration we want to correlate identifiable patterns on the images to accomplish the exact alignment of corresponding objects on the images.

Secondly, we need to make provision for the fact that the sky background is not dark, but has some intensity of its own. This intensity contributes to the intensity of a stellar object and we therefore have to make adjustments to the estimated stellar brightness, which take into account the contamination by the background sky radiation.

Lastly we will address the issue of PSF modelling, to investigate the nature of the stellar object on an image. This will give us some insight into the effect of the earth's atmosphere on the light from the point source on its way to the detector. The turbulent atmosphere causes the light from the point source to be distributed over an extended area, thus representing the source as a blurred stellar object on the image.

Another factor to be considered is the behaviour of the objects that lie close to the edges of an image.

In summary the three basic questions every system has to address are:

1. Registration, which is the alignment of objects on the two images that are being

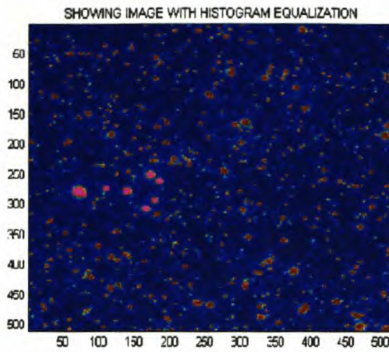


Figure 4.1(a): The reference image.

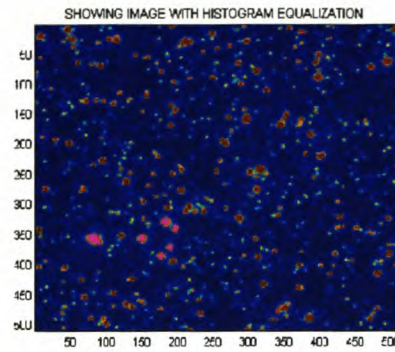


Figure 4.1(b): The comparison image.

compared.

2. Estimation of the background.
3. PSF modelling.

## 4.1 Registration Through Pattern Recognition

To compare the stellar objects on two different images, it is necessary to align the objects on the two images. The importance of good registration can hardly be over-emphasised. If the registration is not good, extra anomalies appear on the residual image, which is the direct result of poor registration.

Figures 4.1(a) and 4.1(b) illustrate the problem — an automated matching of the indicated patterns is required. The two basic methods used for registration are:

1. A triangulation method.
2. Registration using the intersecting points of circles.

### 4.1.1 Problems Encountered with the Images

Let us first consider the data images that we are working with. Recall the different distortions of the images that we need to take into account.

1. Atmospheric dispersion: When observing objects in the visible wavelength range, broad band filters are used. These filters restrict the range of wavelengths reaching

the detector and the resulting effective wavelength of starlight seen by the detector is the results from the convolution of the stellar intensity distribution and the filter passband. For a *v*-filter — a yellow filter which consequently only allows yellow light to pass through it to the detector — the effective wavelength for a blue star would be  $\sim 5400\text{\AA}$  and  $\sim 5500\text{\AA}$  for a red star. The differential refraction of the atmosphere causes different wavelengths to refract at different angles. Consequently at a zenith angle  $z = 45^\circ$  the difference would be  $\sim 0.04''$  and is negligible, but for a zenith angle of  $z = 60^\circ$  the difference is  $0.07''$  which is a significant 0.2 pixels.

2. Stars are appearing and disappearing at the edges, so you never have the same picture on both images. This happens because the telescope is never precisely re-aligned.
3. Misidentification of a field may lead to confusion in the program.
4. The effects of the seeing and the atmosphere (PSF) will influence the quality of the images, such as the number of stars, the profile of the stars, etc.
5. Background radiation, cosmic rays and noise as discussed in the previous chapter.

### 4.1.2 Registration Through Triangulation

The basic idea is that a large number of triangles are drawn between stars on both images. We then use the lengths of the lines (distances between the stars) and the angle between these lines as properties to correlate the corresponding stars on the two images.

First we draw a triangle on the chosen reference image. Then we draw a triangle on the comparison image and compare their properties. This means that we choose a star and draw triangles between it and all the other stars while comparing the properties for each triangle that we draw. This process is illustrated schematically in figure 4.2. Then we move on to the next star and repeat the procedure. It is clearly not feasible to do this using all the stars and we need to scale down on the amount of work and repetition:

1. Set the threshold that is used when the binary image<sup>1</sup> is created, to a higher value. This means that there will be fewer stars on the binary image. Fewer stars mean

---

<sup>1</sup>The binary image is a black and white image of the grayscale sky-image. Conversion is done by setting all the grayscale values lower than some threshold equal to zero and all the other values equal to one.

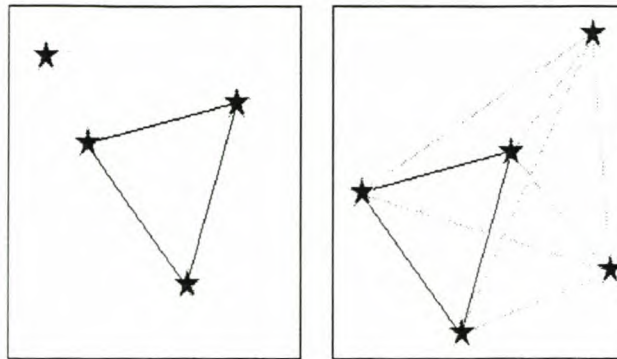


Figure 4.2: Illustration of the basic concept of the triangulation method. The black triangle, in the right-hand figure, indicates the correlated triangle, while the gray triangles indicate the possibilities that exist. Only the three stars framing the black triangles are common to both images, yet a successful registration is possible.

fewer triangles. This can also be accomplished by only considering the brightest stars in the centre of the image.

2. Restrict the stars that are used to build the comparison triangles to stars that are roughly in the same region as the stars that were chosen to create the reference triangles and/or in the same brightness range. This approach works well if the images are very similar and therefore almost correlated. When we start the comparison of the properties of the triangles, we might restrict ourselves to the comparison of the longest distance and the largest angle. This means fewer comparisons. A potential match is verified by comparing the distances and angles between more stars.
3. Store the properties of a triangle once it has been calculated, along with the position of the stars used for the triangle. This will prevent drawing and calculating from the same triangle three times. It will however take up a significant amount of storage (depending on the number of stars).
4. The last suggestion requires some work beforehand, but will be the most economical. When the stars on both images are identified, create two lists containing these stars (one for each sky-image). Sort these lists according to one of the properties of the stellar objects, such as brightness. After drawing the reference triangles, do the first

comparison as suggested in (2) and test only a few properties of the triangles to scale down on the number of comparison triangles. Start the comparison with the comparison triangles nearest to the position of the reference triangle and expand the search area from there. After all the triangles for the first star in the list have been correlated, simply move on to the next star in the list. This will prevent the repetition mentioned in (3).

### 4.1.3 Registration using the Intersection Points of Circles

Instead of trying to match most or all the stars in the two images, our registration is based on the number of the brightest stars that can be identified in the two images. This has the advantage of being fast, without sacrificing too much in terms of robustness.

The centroid of a number of bright stars (10 – 20) are determined and assigned as the positions of the stars. Thus we have the positions of some stars for each image. We use the positions to create two lists (one for each image) and sort them according to brightness. To achieve the correlation of the image, we correlate the two lists by identifying which sets of co-ordinates in the two lists represent the same stellar object. Since the two lists are sorted according to brightness we can restrict the number of stars we are going to consider as correlation candidates.

We start this method in much the same way as the triangulation method and move to a method in which we use the intersection points of circular arcs drawn around two stars to find another (third) star, which will then be correlated on both lists.

A basic algorithm for the method implemented (illustrated in figure 4.3) is:

1. We pick two stars that we have correlated on the two images by using the triangulation step. The numbered stars in figure 4.3 represent these.
2. On the first image, determine the distances of the two chosen stars, to a third star. Since we know the distance of this star to the two reference stars, we can calculate the intersection points of two circles. At one of these intersections lies the third correlation star.
3. Now we use the two correlated reference stars on the second image. We will draw circles around these two stars that have the same radii as determined above. This gives us two intersection points. Located on one of these intersection points will

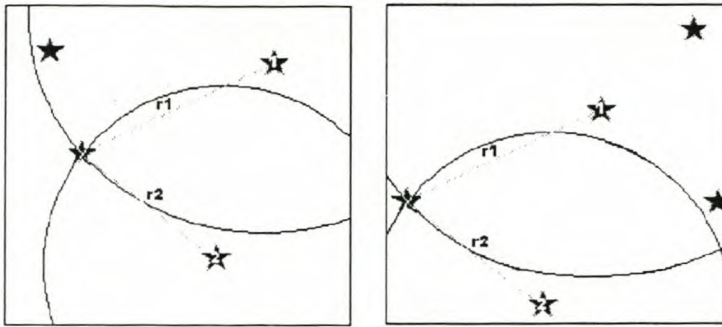


Figure 4.3: Graphical representation of the method of circle intersection used for registration. The numbered stars are the stars identified for the correlation of the rest of the stars. The circles centered on them intersect at the position of a third star on the reference image. This makes it possible to identify the correlated third star on the comparison image, by using the given radii ( $r_1$  and  $r_2$ ).

then be the third star. The distances might vary such as in the case of atmospheric dispersion. These changes are relatively small and allowances are made for these discrepancies.

4. After we have correlated a number of stars (6 – 10), we have enough information to calculate the rotation and translation between the two images.

#### 4.1.4 Remarks

- Note that the first two pairs of stars must be correlated before we can use this method. This is bound to be expensive, but accuracy in this correlation is a necessity. Choose three bright stars on the reference image (close to the center of the image) from the list of objects sorted according to brightness. Since we are now only working with three stars, and therefore one triangle, the method of triangulation will be fast and accurate enough to provide us with a good guess as to the correlation of the first two stars.
- We correlate stars from the dimmer, comparison image, with stars on the brighter, reference image. The reason for this is that there is a greater chance to identify the dimmer stars on the comparison image with stars on the reference image. If we work the other way round, we might find stars on the reference image that is not visible on the comparison image.

The brightest stars on the reference image might be saturated, while this might not be the case on the dimmer comparison image.

- If the registration is not correct, inconsistencies arise and the procedure is repeated.

### 4.1.5 Matching of the Images

All that remains to be done is to match the two images through rotation and translation. This is calculated in two separate steps — iteratively going down intervals of grayscales — using a least squares approach. We do this until the two images are registered as well as this coarse method will allow. (It is seldom necessary to move down more than two interval levels).

1. Translation: We calculate the shift in the  $x$  and  $y$  directions by making use of a simple least squares approximation.
2. Rotation: After translation the rotation between the images is obvious. Usually rotation of centroids is small. (This is mostly due to small mechanical instabilities in the autoguider or changes in the instrumental setup between images.) Again a least squares approach is used to determine the rotation and the centre point of this rotation. Since it is non-linear the least squares solution is calculated using the method of steepest descent. This gives us the angle of rotation and the centre of rotation. It is important to note that the centre of rotation is not necessarily the centre (or corner) of the image.
3. Fine tune the calculations by moving down the list of stars.

The algorithm is repeated until we achieve the best fit that is possible using this method, which is approximately pixel accuracy. The reader is referred to §4.1.6 for an in-depth discussion on the accuracy of this method. The implementation of this method is shown in figures 4.4 – 4.7.





Figure 4.4: Reference image used to register the comparison image to.



Figure 4.5: The comparison image. The difference between the two images is obvious.



Figure 4.6: The comparison image after registration.



Figure 4.7(a): The difference between the reference image and the registered comparison image. The image is displayed as a negative of the absolute value of the result after subtraction to show the pixel accuracy achieved through registration by circle intersection. Also clearly visible on the image is the bottom edge indicating the shift of the comparison image to fit the reference image.

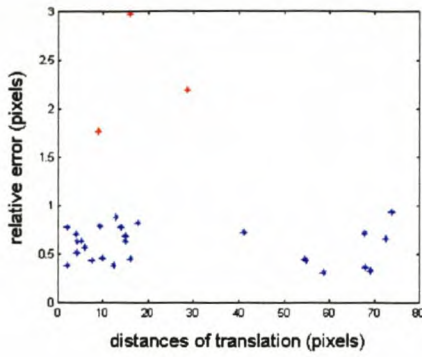


Figure 4.8: The relative error of each image against the respective distances of translation.

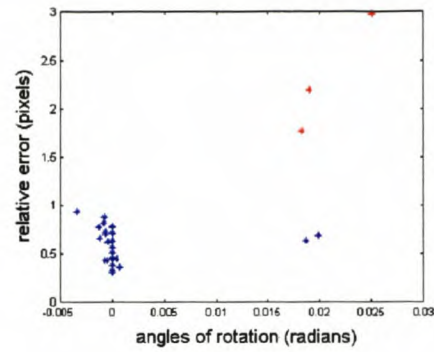


Figure 4.9: The relative error of each image against the respective angles of rotation.

#### 4.1.6 Accuracy of the Registration Technique

To determine how accurate the registration of the two images is, we have to look at the distances (separation) between the positions of the correlated objects on the two images after they have been registered. Thus for each of the correlated objects we determined:

$$r_i = \left[ (X_{1i} - X_{2i})^2 + (Y_{1i} - Y_{2i})^2 \right]^{\frac{1}{2}} \quad (4.1)$$

$$\bar{r} = \frac{1}{N} \sum_{i=1}^N r_i \quad (4.2)$$

$$\sigma_r = \left[ \frac{\sum_{i=1}^N (r_i - \bar{r})^2}{(N - 1)} \right]^{\frac{1}{2}} \quad (4.3)$$

where  $i = 1, \dots, N$  ( $N$  is the number of correlated objects and  $(X_{1i}, Y_{1i})$  and  $(X_{2i}, Y_{2i})$  are the registered positions of the objects)

- Note that  $r_i$  is the error in the registration,  $\bar{r}$  is the mean error and  $\sigma_r$  is the standard deviation.

Using a dataset of 29 images we get  $\sigma_r \sim 0.45$  pixels. For 26 of the images we found that the mean distance was in the order of  $\sim 0.63$  pixels and in three images we found that the relative mean distances were more than one pixel.

Interestingly, figure 4.8 shows that the accuracy of the registration is independent of the translation distance between the images. This is clearly indicated by the blue stars on the

figure. The three red stars are the mean distances of the three images with unsatisfactory registration accuracy.

Figure 4.9 shows the results for the angle of rotation. Note that most of the rotation angles are very small (typically  $< 0.005$ ). We find some rotation angles with larger values and all of the unsatisfactory errors are situated in this region of large rotation angles.

This indicates that bad registration might be caused by excessive rotation. This is caused by non-linear distortions that are not easily corrected by linear methods.

#### 4.1.7 Comparison of the Two Registration Techniques

The programs were run on a Pentium II PC with 400 MHz processor and 128MB RAM. The processing time depends on how close the two images are initially. The triangulation method takes anything on the order of 40 to 900 seconds to register two images, while the intersection method takes approximately 40 to 100 seconds. Note that emphasis should be placed on the relative differences in processing time and not on the actual times, since the code was not optimised in both methods and the MATLAB program is slow.

The second method of circle intersection is more efficient in terms of processing time required. Most of the computational cost goes into the triangulation step that is used to correlate the first two specific stars. There is no unnecessary data that need to be stored, which leaves us with a minimal amount of additional storage. Once two stars are correlated, they can be taken out of the list, which reduces the number of tests that need to be performed. Furthermore, the choice of stars is restricted to only a few within restrictive brightness boundaries. Thus we see that the lists of positions provide all that is needed to perform the necessary calculations. Another point of interest is the ease of automating our method and portability has posed no problem when applying our method.

#### 4.1.8 Possible Future Expansion

After the first two stars have been identified correctly, the rest of the circle intersection method is fast. The main drawback to this method is the fact that it is highly dependent on the accurate correlation of the first two stars. That is why a method such as triangulation (which has already proven itself in astronomical applications) is used to do this correlation. However, one learns very quickly if the first attempt of registration is incorrect (such as in the case of mirror image). It is a simple matter of choosing another candidate and

repeating the procedure.

Limited scale changes can be handled. Again this is something that only needs to be addressed during the first step of triangulation. This step may now need to be expanded a little to give enough data to calculate the relative differences in scale. This can then be applied directly to the radii of the circles to compensate and to determine the right intersection point for accurate correlation.

## 4.2 Subpixel Registration using Interpolation

The method discussed above allows for pixel accuracy, since it only allows for linear deformations — translation and rotation. Now we have to consider local non-linear corrections.

### 4.2.1 Basic Description and Approach

Given two registered images — using the intersection approach discussed above — the positions of the stars are known to within pixel accuracy. Find correlated isolated stars on both images. They are not perfectly aligned in general and we correct their alignment. Linear interpolation then provides an improved registration of all objects in the vicinity.

In summary:

1. Find isolated stars throughout the two images and force their correlated centres of mass to coincide.
2. All the remaining pixels are moved through linear interpolation,

$$X = P_x(x, y) = Ax + By + C \quad (4.4)$$

$$Y = P_y(x, y) = A'x + B'y + C', \quad (4.5)$$

where  $A, B, C, A', B', C'$  are given by the vertices (isolated stars) of the triangle.

It is straightforward to calculate the three parameters from the three interpolation points of each triangle.

The solution obtained during implementation of this technique was satisfactory. The registration errors are reduced to the third decimal. When viewing the differences of the images after sub-pixel registration we see only gray remaining.

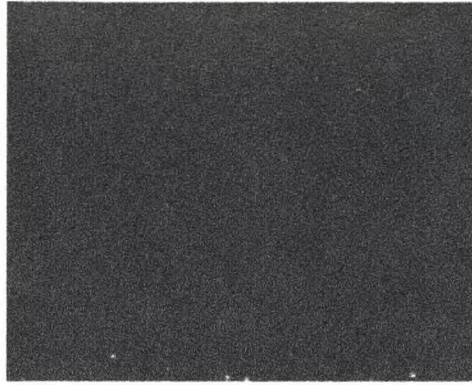


Figure 4.7(b): The differences between the reference image and the registered comparison image.

### 4.3 Sky Background Determination and Removal

As mentioned previously, the sky background is not zero, but has its own radiation [Hopkins 1980]. Other contributors may also include very faint stars so near to the sky background that they cannot be distinguished from it as well as light from sources such as the moon that is scattered by the atmosphere. Though most of these effects might be difficult to see when viewing the image, the information is still present in the image matrix. Thus if one wants to compare two images, one also has to take into account these inherent differences. We need to get rid of these differences as best we can. A standard practice in astronomy is to get rid of the background by ‘subtracting’ it from the image. A common way of doing this is by fitting a plane through the image and then ‘subtracting’ it [Schechter et. al. 1993]. This once-off approach is fast and efficient enough to be used in most cases. For the ‘subtraction’ of the background in this application we used a strategy that was mentioned in a paper for a different type of application [Smith 1996].

The idea is to first remove the coarsest and most obvious parts of the background and then work down to the finer more subtle parts. However we remove the fainter parts first, since the fainter objects have too much background contamination to contain any information, and leave the more obvious parts for later.

#### 4.3.1 Discussion of the Method

This method uses three steps:

1. First a histogram is used to find a threshold value to use as a cut-off for the lower

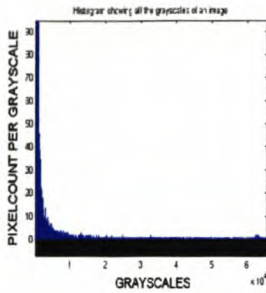


Figure 4.10(a): A histogram of the brightness values.

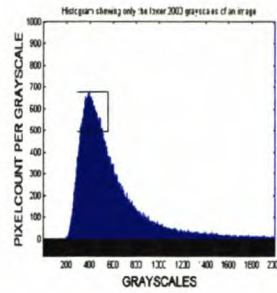


Figure 4.10(b): The lower grayscale values show the definite maximum that exists there. The box indicates the grayscales at the maximum through which the quadratic spline was fitted.

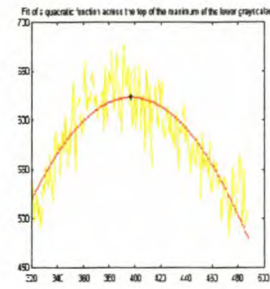


Figure 4.10(c): The quadratic spline fitted over the maximum formed in the lower grayscales (see box in (b)).

brightness values in the image. We are working with images that are semi-crowded and most of the objects lie close to the background. This is shown clearly when we look at a histogram of the brightness values on the images, figure 4.10(a).

These low brightness values makes it impossible to isolate these stars for background calculation. Figure 4.10(a) shows that almost all the pixels on the image have values that are located in the lower grayscales. These lower grayscales display a very definite maximum on figure 4.10(b). The assumption is made that the most common pixel intensity in the image is approximately at the level of the background. Therefore we build a histogram of pixel intensities and find the peak value by means of a quadratic spline fitted over these values. The width of the histogram is determined under the assumption that the histogram is Gaussian.

In the case of a crowded field user defined boxes are used to identify possible regions that can be used.

To determine the threshold we now apply a quadratic least squares fit over the part of the distribution containing the maximum values on figure 4.10(c).

Using the fitted function it is possible to determine the maximum value of the distribution and this is the value that it used as a threshold.

This method has been implemented in a program available on the Internet at [astro.nmsu.edu/~holtz/xvista/help/man/sky.html](http://astro.nmsu.edu/~holtz/xvista/help/man/sky.html).

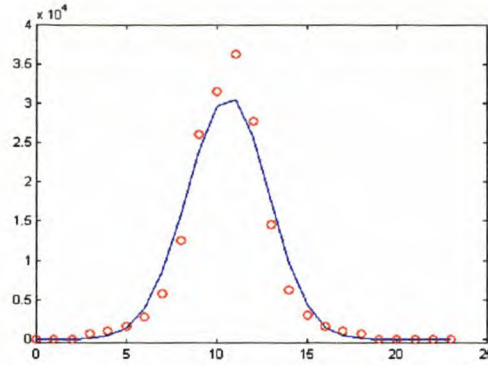


Figure 4.11: An intersection through an isolated star was taken, with the circles (o) indicating the intensity values at each gridpoint of that intersection. A cubic smoothing spline is fitted through these points as indicated by the solid line.

Since the data images are semi-crowded we end up with a low threshold brightness value. Thus applying the threshold should in fact remove the minimum amount of background from the image. This already leads to an improved isolation of the objects on the image, especially the fainter objects. This in turn is useful for the application of the next step of background estimation, which uses these isolated objects.

2. Plane Fitting: Identifying some of the brighter, isolated stars distributed over the whole of the image, we determine the background around each one. It is only necessary to follow the star from the peak intensity until it flattens out. This is achieved by making four intersections through the star (vertically, horizontally and two diagonal intersections) and then fitting a cubic smoothing spline ([De Boor 1963] and [Herbst 1999]) through each of the intensity curves (as shown in figure 4.11) and finding the position where the first and second derivatives become zero.

When the flat regions have been identified, a square annulus is fitted around the star. This technique is only applicable to more sparsely populated fields [Da Costa 1992]. The background values identified for each star are then used to construct a plane through the image, using a least squares approximation. This plane gives an approximation of the sky background over the whole image. It should allow for a small gradient, which may be caused for example by light from the moon that is scattered by the atmosphere. This plane fitting technique could be made more precise by doing the plane fitting for small parts of the image, since this method aims to estimate the background of the image as accurately as possible.

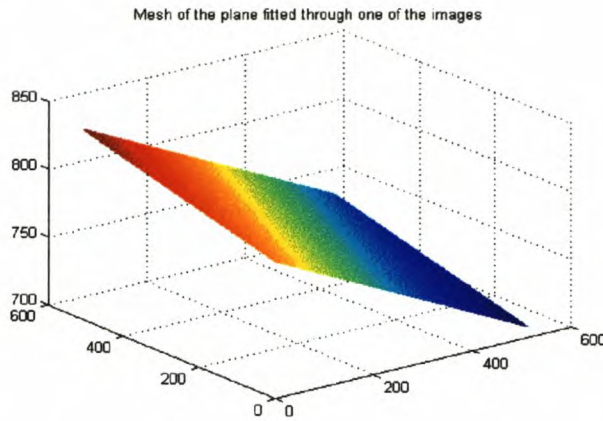


Figure 4.12: The plane, approximating the background.

A typical plane is shown in figure 4.12.

We do not remove this plane from the image directly, but rather keep it as an approximation to be used during the local background analysis in the next step. If one wishes to investigate the profile of the star, one could use this plane to smooth out the background.

3. Investigation of individual stars: Later when the stellar object is investigated in detail, a further estimation of the local background in the immediate vicinity of the object itself is made. This is necessitated by the fact that the object might not be isolated any more. This problem is considerably harder. In the next section the watershedding algorithm is described for this purpose.

## 4.4 Watershedding

We find that with crowded stellar images or with images containing dim objects, it becomes much more difficult to automate the finding and isolation of stellar objects and also to determine the cut-off for the background value.

In an attempt to get away from the dependence on isolated stars to determine values for the background plane, we investigated the watershedding algorithm.

The idea behind watershedding is straightforward and easy to understand [Vincent 1991].



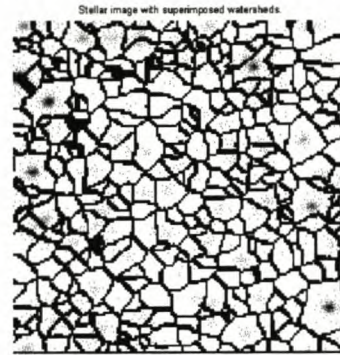
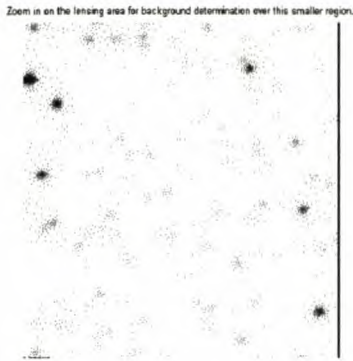


Figure 4.13(a): Enlargement of part of the image to show the lensing event area.

Figure 4.13(b): Image with the watersheds superimposed on it.

Imagine the stellar objects on the image as sunken valleys on a flat landscape. In other words, we regard the image to be a topographic surface with different levels of minima. (If necessary we invert the images so that the higher intensities corresponds to the lower grayscale values.) Pierce holes in each local minimum, then slowly immerse the surface into water. Starting from the minima of lowest altitude, the water will progressively fill up the different valleys of the image. At positions where the water coming from two different minima merges, build a wall. At the end these walls, which corresponds to the watersheds of the image, will surround all the minima.

Figures 4.13(a) and 4.13(b) show part of the image as well as the result of the watershed algorithm. Although figure 4.13(b) is highly over segmented, this is of no consequence in this application. The point is that the boundaries tend to run through background values.

Thus, if we can identify the watersheds that go across the background regions, we can identify the background values. This provides us with a very large spread of pixels and values across the whole image that we can use to fit the plane through.

All we do now is to identify all the watershed pixels and calculate a histogram for the image.

To determine the background we look at the histogram of the plot in figure 4.14. It clearly shows the region where the maximum number of pixels is situated. All the pixels that lie below the threshold in figure 4.14 are considered to be background pixels. This leaves us with an average of  $\pm 12000$  background pixels taken from the image compared to the

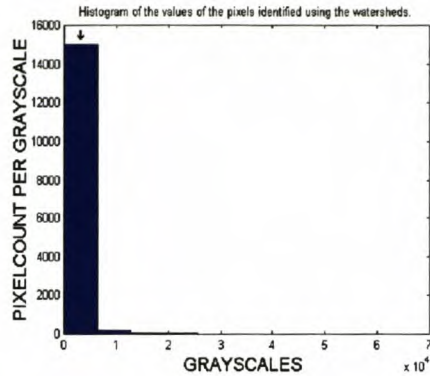


Figure 4.14: The histogram shows the maximum amount of pixels to be at the lowest values.

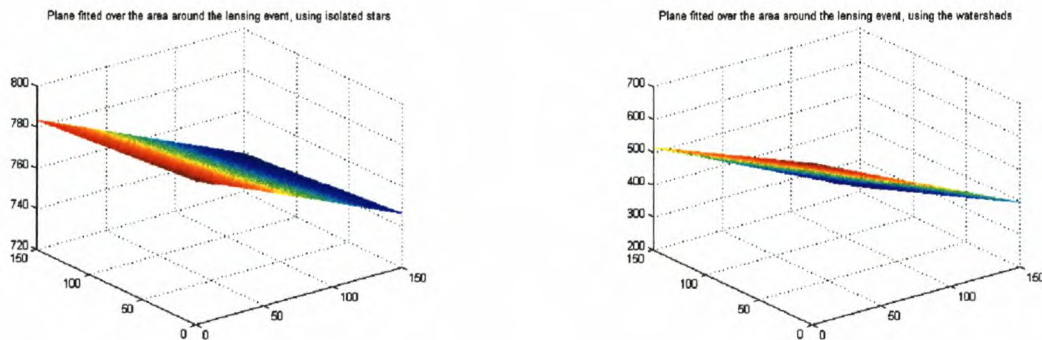


Figure 4.15: Plane fitted over the image using the background determined around isolated stars. Figure 4.16: Plane fitted over the images using the background determined through use of the watersheds.

$\pm 4\,000$  pixels we got after using the object isolation method.

We now use all the identified pixels and their values to compose the input data for the plane that will be fitted over the image. Since we now have a wider spread of pixels and values over the whole of the image, the plane that is fitted is a closer representation to the behaviour and value of the background over the image, than the plane that was calculated using only a few stars.

If we compare the two planes (in figure 4.15 and 4.16) we see that both gradients are in the same direction. The first plane (figure 4.15) is tilted slightly more than the second (figure 4.16), but there is virtually no noticeable difference between the two planes. The second method is recommended because it does not require extra input, isolated stars, or sparsely populated stellar fields. One might even go further and develop a simple model for the

background that will be a closer representation than a plane. High accuracy modelling of the sky background brightness is of particular importance in large scale surveys such as the Sloan Digital Sky Survey [Gunn 1995], since most objects will be close to the detection limit.

Watershedding is an excellent method for the segmentation of an image. Our image is over-segmented, but this can be corrected. After this kind of correction one will be left with an image showing all the stellar objects in their respective isolated regions. A few remarks are in order:

- Bigger regions show more isolated objects: This might be useful to identify isolated stars in sparsely populated stellar fields, by comparing relative regional sizes. As well as the fact that the regions around these stars are identified for extraction or use in calculations.
- Bright stars are identified and isolated: In our application the bright stars are mostly considered for the approximation of the background values. Just as in the previous case they are now isolated for use with an annulus already drawn. Also if one wants to discard or remove these objects to investigate only the dimmer objects, this can now be done with ease.
- Stars lying next to each other are separated: This is useful if one is not fitting models to the stellar profiles to determine their brightness, but rather wants to approximate the brightness values of the stars in a more direct way.
- Optimal region of removal for saturated stars are indicated: Saturated stars are normally ignored since they are not considered to give any useful information. Mostly these stars are removed from the images before analysis. This segmentation method identifies and gives an optimal region around the star to be removed to ensure that the minimal amount of influence from these saturated objects is retained on the image. Since this method of segmentation is easy to automate, the regions for the saturated star is identified for all the images that might be used in the analysis. Even if the object is not saturated on one of the images, the position and influence region is identified and can be removed.

## 4.5 Point Spread Function (PSF) Modelling

There are a number of approaches describing PSF modelling available in the literature. For example [Schechter et. al. 1993] uses parametric model fitting, which has difficulty fitting both the top and the wings of the intensity distribution using only one model. [Howell 1989] uses profile fitting of the data, which requires a lot more work for a small amount of accuracy gained.

Though there exist a few equations and descriptions for this PSF [Stetson et. al. 1986], there are no clear solutions. Generally the intensity distributions is assumed to be a Gaussian distribution.

In these parametric methods a specific functional form (such as a Gaussian) is assumed for the density model. This contains a number of parameters that are then optimised by fitting the model to the data set. The biggest drawback is the fact that the parametric function chosen might not be a good representation of the real density. This drawback can greatly be overcome by the use of a Gaussian mixture model. Though this will be more calculation intensive, it would be a preferable approach if one uses parametric methods. There are other options available. We will name but not discuss them, since we believe that parametric methods will provide models with sufficient accuracy. Alternative models are:

- (i) Non-parametric estimation.
- (ii) Semi-parametric estimations.

Since the only relevant information on the image is the intensities of the stars there should be as little processing as possible of the images.

Figure 4.17 and figure 4.18 shows a typical PSF profile of a star. Note the apparent Gaussian distribution.

It is however very important that when we refer to figure 4.17 and figure 4.18, we must remember that in displaying the data, various degrees of smoothing were inflicted on the data by the display program, and this gives rise to these simple output figures. Our normal distribution function will thus be an approximation of the intensity distribution as seen in figure 4.17. Saturated stars have lost information and do not fit the Gaussian models.

In practice, the normal distribution function works rather well, with differences usually occurring when trying to fit the top and wings using one equation. There tends to be

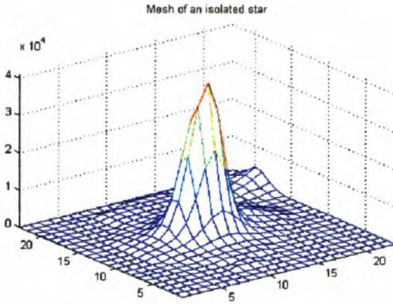


Figure 4.17: A mesh from one of the isolated stars that was used to determine the background plane. The other star, partly visible on the image, is far enough removed so that its light does not have a significant influence on the profile.

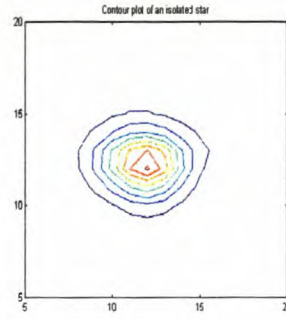


Figure 4.18: A contour plot of the same star used in the mesh of the previous figure. The shape of the contours clearly indicate a normal density distribution function.

spillover on the wings when the top is fitted correctly and the same for the top when the wings are fitted. Thus for our experimentation we have restricted ourselves to well isolated stars.

## 4.6 Normal Density Distribution Function

The PSF of a stellar object can typically be modelled with a Gaussian distribution. This suggests that a Gaussian filter may be appropriate for the matching of different stellar images as described by image subtraction [Alard 1997]. Let us consider a basic approach.

In order to fit a PSF consider the multivariate normal probability density in  $d$  dimensions:

$$p(\mathbf{x}) = \frac{1}{(2\pi)^{\frac{d}{2}} |\Sigma|^{\frac{1}{2}}} \cdot \exp \left[ \frac{1}{2} (\mathbf{x} - \mu)^T \Sigma^{-1} (\mathbf{x} - \mu) \right]. \quad (4.6)$$

Here  $\mu$  is the  $d$ -dimensional mean vector,  $\Sigma$  is a  $d \times d$  dimensional covariance matrix,  $|\Sigma|$  is the determinant of  $\Sigma$  and  $(\mathbf{x} - \mu)^T$  denotes the transpose of the vector  $(\mathbf{x} - \mu)$ ,

$$\mu = E[\mathbf{x}] = \int_{-\infty}^{\infty} p(\mathbf{x}) \mathbf{x} d\mathbf{x} \quad (4.7)$$

and

$$\Sigma = E \left[ (\mathbf{x} - \mu)(\mathbf{x} - \mu)^T \right] = \int_{-\infty}^{\infty} (\mathbf{x} - \mu)(\mathbf{x} - \mu)^T p(\mathbf{x}) d\mathbf{x}. \quad (4.8)$$

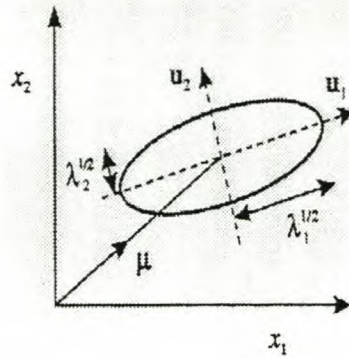


Figure 4.19: A normal distribution in two dimensions is governed by a mean vector  $\mu$  and a covariance matrix with eigenvectors  $\mathbf{u}_1$  and  $\mathbf{u}_2$ , and the corresponding eigenvalues  $\lambda_1$  and  $\lambda_2$ . The ellipse corresponds to a contour of constant probability density on which the density is smaller by a factor  $e^{\frac{1}{2}}$  than it is at the point  $\mu$ .

The factor  $(\mathbf{x} - \mu)^T \Sigma^{-1} (\mathbf{x} - \mu)$  from equation (4.6) is called the Mahalanobis [Bishop 1998] distance from  $\mathbf{x}$  to  $\mu$ .  $E[.]$  denotes the expectation.

Here the principal axes of the hyperellipsoids (figure 4.24) are given by the eigenvectors  $\mathbf{u}_i$  of  $\Sigma$ .

Now let us consider this as a filter candidate ( $K$ ) as suggested in [Bishop 1998]. We use a least squares approximation of  $\min \|I - R * K\|^2$  (where  $R$  is the reference image,  $I$  is the comparison image and  $*$  denotes convolution) to obtain the best fitting filter

$$\epsilon = \|I - R * K\|^2. \quad (4.9)$$

After determining  $K$  we can simply convolve our reference image to simulate the stellar profiles of the comparison image which we want to compare.

Although it is possible to find a good match for a single object, it is not possible to do this for a large number of objects, as a Gaussian on a typical image. This is because a Gaussian distribution function does not provide enough degrees of freedom, as is shown in figures 4.20 to 4.22. Consequently astronomers do not use a Gaussian distribution function, but some rational approximation, which provided more free parameters for a better fit.

Since we opted for a more direct approach of signal comparison (see chapter 6), there was no need to pursue this matter.

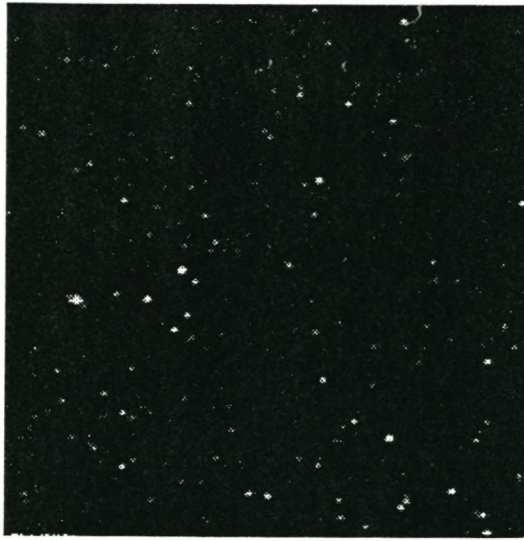


Figure 4.20: The reference image that needs to be softened.

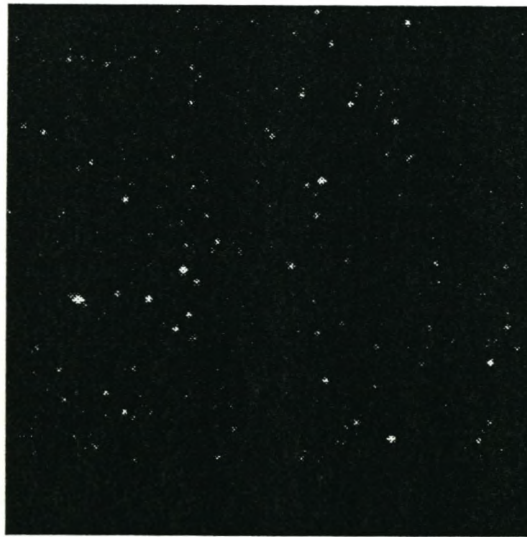


Figure 4.21: The comparison image that we want to simulate by softening the reference image.

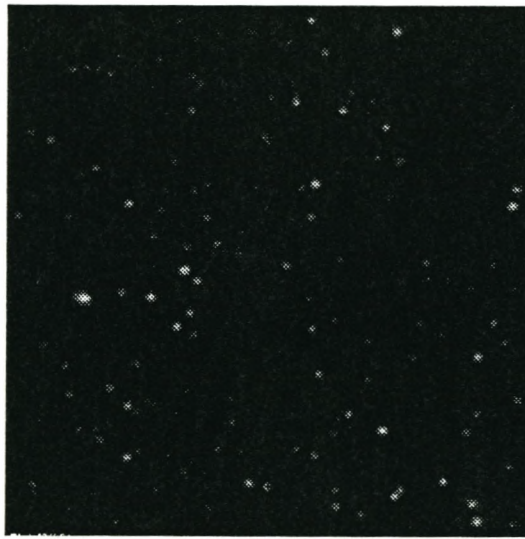


Figure 4.22: The reference image after softening by application of the Gaussian filter. The image is obviously dimmed too much.



## Chapter 5

# Data Extraction and Analysis: Theoretical Background

To do the data extraction and analysis of the lensing event we use various techniques. What we are investigating is methods that are able to identify and analyse the trend in any signal as well as anomalies (such as a blip). We proceed to give the theoretical background of the methods we use to obtain the results presented in chapter 6. Our emphasis is on the methods of wavelet analysis and Locally Weighted Regression (LOESS).

### 5.1 Wavelets

It would take us too far afield to give a detailed description of wavelets, see e.g. [Misiti et. al. 1996] and [Strang 1997]. Let it suffice to say that one way of modelling a wavelet decomposition is to decompose a signal into high and low frequency components, using an appropriate filter bank. The filter bank is carefully constructed to have several desirable features — accuracy, (sometimes) orthogonality and of course perfect reconstruction. The decomposition is done recursively.

All the main ideas are illustrated using the simple Haar filter:

Given a signal  $x_n$ , we can compute a wavelet decomposition by iteratively applying two filters; in the case of the Haar filter, given by

$$\text{Low pass filter: } a_n = \frac{1}{\sqrt{2}}(x_n + x_{n-1})$$

$$\text{High pass filter: } b_n = \frac{1}{\sqrt{2}}(x_n - x_{n-1})$$

Used in this way we end up with two signals, each as long as the original which indicates

a redundancy. In fact we only need to keep every second entry in both signal  $a_n$  and  $b_n$ . This is called downsampling.

Thus we define

$$y_n = a_{2n} := \frac{1}{\sqrt{2}}(x_{2n} + x_{2n-1})$$

$$z_n = b_{2n} := \frac{1}{\sqrt{2}}(x_{2n} - x_{2n-1})$$

and iteratively repeat the process for  $y_n$  and  $z_n$ .

It is instructive to write this in matrix notation.

Assuming a periodic signal, i.e.  $x_n = x_{n+k}$ . Then we can write  $\mathbf{a} = C\mathbf{x}$ , with

$$C = \frac{1}{\sqrt{2}} \begin{bmatrix} 1 & 0 & \dots & \dots & 0 & 1 \\ 1 & 1 & 0 & \dots & \dots & 0 \\ \dots & \dots & 1 & 1 & \dots & \dots \\ 1 & 0 & \dots & \dots & \dots & 1 \end{bmatrix}$$

and  $\mathbf{b} = B\mathbf{x}$ , with

$$B = \frac{1}{\sqrt{2}} \begin{bmatrix} 1 & 0 & \dots & \dots & 0 & -1 \\ -1 & 1 & 0 & \dots & 0 & 0 \\ \dots & \dots & -1 & 1 & \dots & \dots \\ 1 & 0 & \dots & \dots & \dots & -1 \end{bmatrix}$$

Removing the redundancy we find  $\mathbf{y} = L\mathbf{x}$ , with

$$L = (\downarrow 2)C = \frac{1}{\sqrt{2}} \begin{bmatrix} 1 & 0 & \dots & \dots & 0 & 1 \\ 1 & 1 & 0 & \dots & 0 & 0 \\ \dots & \dots & 1 & 1 & \dots & \dots \\ 1 & 0 & \dots & \dots & \dots & 1 \end{bmatrix}$$

and  $\mathbf{z} = D\mathbf{x}$ , with

$$D = (\downarrow 2)B = \frac{1}{\sqrt{2}} \begin{bmatrix} 1 & 0 & \dots & \dots & 0 & -1 \\ -1 & 1 & 0 & \dots & 0 & \dots \\ \dots & \dots & -1 & 1 & \dots & \dots \\ 1 & 0 & \dots & \dots & \dots & -1 \end{bmatrix}$$

By combining the matrices we can calculate  $\mathbf{y}$  and  $\mathbf{z}$ :

$$\begin{bmatrix} y \\ z \end{bmatrix} = \begin{bmatrix} L \\ D \end{bmatrix} \mathbf{x}, \text{ with } \begin{bmatrix} L \\ D \end{bmatrix} \text{ invertible.}$$

- Note that  $L$  and  $D$  are not invertible, but together they are.

$$\text{Thus by inverting } \begin{bmatrix} L \\ D \end{bmatrix} \text{ we get: } \begin{bmatrix} L^T & D^T \end{bmatrix} \begin{bmatrix} L \\ D \end{bmatrix} = L^T L + D^T D = I$$

This expression (called the partition of unity) allows for the decomposition of signal  $x$ :

$$L^T Lx + D^T Dx = x.$$

Thus it follows that  $x$  is reconstructed by:

$$L^T \mathbf{y} + B^T \mathbf{z} = \mathbf{x}$$

Example:

$$\begin{aligned} \mathbf{x} &= [\dots 0 \quad -1 \quad -1 \quad -1 \quad 0 \quad 1 \quad 1 \quad 1 \quad 0 \quad \dots]^T \\ \mathbf{a}^{(1)} &= [\dots \frac{1}{\sqrt{2}} \quad -\frac{1}{\sqrt{2}} \quad -\sqrt{2} \quad -\sqrt{2} \quad -\frac{1}{\sqrt{2}} \quad \frac{1}{\sqrt{2}} \quad \sqrt{2} \quad \sqrt{2} \quad \dots]^T \\ \mathbf{b}^{(1)} &= [\dots -\frac{1}{\sqrt{2}} \quad -\frac{1}{\sqrt{2}} \quad 0 \quad 0 \quad \frac{1}{\sqrt{2}} \quad \frac{1}{\sqrt{2}} \quad 0 \quad 0 \quad \dots]^T \end{aligned}$$

Decimation:

$$\begin{aligned} \mathbf{y}^{(1)} &= [\dots \frac{1}{\sqrt{2}} \quad -\sqrt{2} \quad -\frac{1}{\sqrt{2}} \quad \sqrt{2} \quad \dots]^T \\ \mathbf{z}^{(1)} &= [\dots -\frac{1}{\sqrt{2}} \quad 0 \quad \frac{1}{\sqrt{2}} \quad 0 \quad \dots]^T \end{aligned}$$

Reconstruction:

$$\begin{aligned} \mathbf{x}_{2n} &= [\dots 0 \quad -1 \quad 0 \quad 1 \quad 0 \quad \dots]^T \\ \mathbf{x}_{2n+1} &= [\dots -1 \quad -1 \quad 1 \quad 1 \quad \dots]^T \\ \mathbf{x} &= [\dots 0 \quad -1 \quad -1 \quad -1 \quad 0 \quad 1 \quad 1 \quad 1 \quad 0 \quad \dots]^T \end{aligned}$$

The process is repeated starting from  $\mathbf{y}^{(1)}$ . Where  $\mathbf{y}^{(1)}$  is a smoothed version of  $\mathbf{x}$

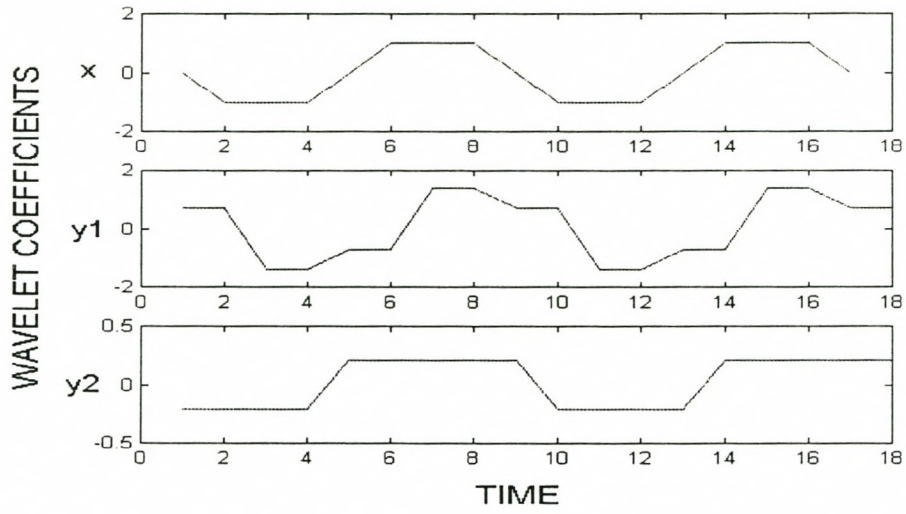
$$\begin{aligned} \mathbf{x}^{(1)} &= [\dots \frac{1}{\sqrt{2}} \quad -\sqrt{2} \quad -\frac{1}{\sqrt{2}} \quad \sqrt{2} \quad \dots]^T \\ \mathbf{a}^{(2)} &= [\dots \frac{1-\sqrt{2}}{2} \quad \frac{-1-\sqrt{2}}{2} \quad \frac{\sqrt{2}-1}{2} \quad \frac{1+\sqrt{2}}{2} \quad \dots]^T \\ \mathbf{b}^{(2)} &= [\dots \frac{-1-\sqrt{2}}{2} \quad \frac{\sqrt{2}-1}{2} \quad \frac{1+\sqrt{2}}{2} \quad \frac{1-\sqrt{2}}{2} \quad \dots]^T \end{aligned}$$

Decimation:

$$\begin{aligned} \mathbf{y}^{(2)} &= [\dots \frac{1-\sqrt{2}}{2} \quad \frac{\sqrt{2}-1}{2} \quad \dots]^T \\ \mathbf{z}^{(2)} &= [\dots \frac{-1-\sqrt{2}}{2} \quad \frac{1+\sqrt{2}}{2} \quad \dots]^T \end{aligned}$$

Repeat the processing of  $\mathbf{y}^{(n)}$  iteratively.

The smoothing of the signal is shown in the following graph:



Graph showing the smoothing of the signal  $x$  through two steps of wavelet decomposition.

Although the Haar filter contains many of the basic ideas it is simply not accurate enough for most applications. Daubechies constructed a whole hierarchy of filters that will exactly reproduce polynomials of higher order. Wavelet analysis is capable of revealing aspects of data such as trends, breakdown points, discontinuities in higher derivatives and self-similarity. They can also compress or de-noise signals, often without much degradation.

## 5.2 General Trend

We calculate a general trend using the signals from the reference stars, which show no fluctuations in brightness except for the distortions on the image. We then use this trend for the comparison of our signals.

The calculation of this general trend is an iterative calculation with  $T$ =number of time points and  $N$ =number of signals.

Algorithm:

1. First guess for the general trend is usually the mean of the signals

$$\bar{X}(t) = \frac{1}{N} \sum_{j=1}^N X_j(t) , \quad t = 1, \dots, T , \quad (5.1)$$

and  $X_j$  the data points on the signal.

2. Calculate the offsets of all the reference signals from the calculated trend

$$X'_j(t) = X_j(t) - \bar{X}(t) , \quad t = 1, \dots, T \text{ and } j = 1, \dots, N . \quad (5.2)$$

3. Determine the spread of the reference signals around the mean

$$\sigma_j^2 = \frac{1}{T-1} \sum_{t=1}^T [X'_j(t)]^2 , \quad j = 1, \dots, N . \quad (5.3)$$

4. Calculate the new general trend

$$\bar{X}(t) = \frac{\sum_{j=1}^N \frac{X_j(t)}{\sigma_j^2}}{\sum_{j=1}^N \frac{1}{\sigma_j^2}} , \quad t = 1, \dots, T . \quad (5.4)$$

5. Iteratively repeat steps 2 to 4.

This method will usually converge rapidly and it is seldom necessary to do more than two or so iterations, depending on the reference signals. After we have calculated the general trend, we subtract all the signals from this trend. We expect to find that the residual signals ( $X_j'$ ) will be spread around zero and we look for those signals that show different behaviour.

### 5.3 (Robust) Locally Weighted Regression (LOESS)

Locally weighted regression is a procedure for fitting a regression surface to data through smoothing. The dependent variable is smoothed as a function of the independent variables in a moving fashion analogous to how a moving average is computed for a time series [Cleveland et. al. 1988].

Robust locally weighted regression is a method for smoothing a scatter plot,  $(x_i, y_i)$ ,  $i = 1, \dots, N$ , in which the fitted value at  $x_k$  is the value of a polynomial fit to the data, using weighted least squares, where the weight for  $(x_i, y_i)$  is larger if  $x_i$  is close to  $x_k$  and small if it is not [Cleveland 1979].

In addition, the robust fitting procedure guards against deviant points distorting the smooth fit. The smoothing of scatter plots entails the formation of new points  $(x_i, y_i')$  which portrays the location of the distribution of the variable on the vertical axis ( $Y$ ), given the value of the variable on the horizontal axis ( $X = x_i$ ). Thus the point  $(x_i, y_i')$  is called the smoothed points at  $x_i$  and  $y_i'$  is the fitted value at  $x_i$ .

Basic framework:

For each  $x_i$ , the weights,  $w_k(x_i)$ , are defined for all  $x_k$ ,  $k = 1, \dots, n$ , using a weight function ( $W$ ), by centring  $W$  at  $x_i$  and scaling it so that the point at which  $W$  first becomes zero is at the  $r^{\text{th}}$  nearest neighbour of  $x_i$ . The initial fitted value ( $y_i'$ ) at  $x_i$  is the value given by a  $d^{\text{th}}$  degree polynomial fitted to the data using weighted least squares. This procedure for computing the initial fitted values is called locally weighted regression.

Define a different set of weights ( $\delta_i$ ) for each  $(x_i, y_i)$  based on the size of the residual  $(y_i - y_i')$ . Small weights are assigned to large residuals and larger weights to smaller residuals. New fitted values are computed using the new weights. Iterate the computation of new weights and new fitted values. This is called robust locally weighted regression.

For the smoothness procedure use

$$y_i = g(x_i) + \epsilon_i \quad (5.5)$$

with  $\epsilon_i \sim N[0, \sigma^2]$  and  $g$  a smooth function of the independent variables. In other words  $y_i'$  is an estimate of  $g(x_i)$  and the assumption of smoothness allows points in the neighbourhood of  $(x_i, y_i)$  to be used in the calculation of  $y_i'$ . Lastly, let  $f$  be the fraction of data included in the smoothing window, thus  $0 < f \leq 1$ , with an increase in  $f$  leading to an increase in the smoothness of the smoothed points  $(x_i, y_i')$ . The goal in the choice of  $f$  is to pick a value as large as possible to minimise the variability in the smoothed points, without distorting the pattern in the data.

The procedure:

1. Compute the estimates  $\beta'_j(x_i)$ ,  $j = 0, \dots, d$ , of the parameters of the polynomial (of degree  $d$ ) fitted by weighted least squares, with weight  $w_k(x_i)$  for  $(x_i, y_i)$

$$\beta'_j(x_i) = \min \left[ \sum_{k=1}^n w_k(x_i) (y_k - \beta_0 - \beta_1 x_k - \dots - \beta_d x_k^d)^2 \right]. \quad (5.6)$$

The smoothed point at  $x_i$  where  $y_i'$  is the fitted value of the regression at  $x_i$

$$y'_i = \sum_{j=0}^d \beta'_j(x_i) x_i^j = \sum_{k=1}^n r_k(x_i) y_k \quad (5.7)$$

where  $r_k(x_i)$  are the coefficients for the  $y_k$  that arise from the regression.

2. Define a bi-square weight function ( $B$ )

$$B(x) = \begin{cases} (1 - x^2)^2 & : |x| < 1 \\ 0 & : |x| \geq 1 \end{cases} \quad (5.8)$$

and  $e_i = y_i - y_i'$  the residual from the current fitted values.

Define robust weights

$$\delta_k = B\left(\frac{e_k}{6s}\right) \quad (5.9)$$

where  $s$  is the median of  $|e_i|$ .

3. Compute new  $y'_i$  for each  $i$  by fitting a  $d^{\text{th}}$  degree polynomial using weighted least squares with weight  $\delta_k w_k(x_i)$  at  $(x_k, y_k)$ .
4. Iterate step 2 and 3. The final  $y'_i$  are the robust locally weighted regression fitted values.

## Chapter 6

# Data Analysis and Results

On the images provided by the PLANET collaboration the lensing event is already identified. Thus we will only concentrate on the analysis of the light curve in this chapter.

For our analysis we took a small area of  $150 \times 150$  pixels (containing the lensing event) of each of the images. In practice a large image will be divided into smaller pieces, and each piece will be processed independently. Since the images we are interested in are very sparsely populated, we will only use isolated objects as data. This means that our objects will experience no influence from nearby objects. We wish to detect and analyse the changes in intensity of the object through a series of images (figure 6.1). To compensate for possible transparency and seeing variations, the brightness of a possibly variable star should be measured relative to nearby stars.

For our analysis we have to address two issues:

- Identify the trend of the curve, to use for both identification and classification.
- Find any anomalies, such as a blip<sup>1</sup>, that might appear in the data.

To do the analysis we investigate various techniques. What we are looking for is a method that will be able to address both issues successfully.

We apply these methods to the real data as well as to artificial data, to show the efficiency of the methods when applied to various types of data. For the analysis of the data signals we use four different methods:

---

<sup>1</sup>A blip is an anomaly on a signal that over a short timescale show some significant departure from the expected smooth trend.



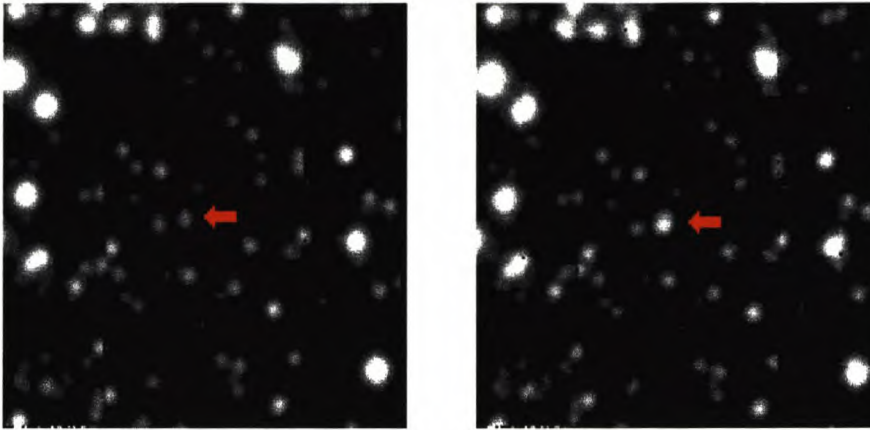


Figure 6.1: Two images showing the increase in the intensity of the lensing object. The first image was taken from very early in the series of data images and the second was taken from near the end. The red arrow indicates the lensing event, which clearly show an increase in intensity.

1. Data subtraction — the subtraction of the signals from each other.
2. Wavelets
3. The determination of a general trend.
4. Locally weighted regression, a statistical method of analysing data.

## 6.1 Intensity Variations

We have chosen three objects from the reference image. One of the objects is the identified lensing event, showing a significant brightness variation. However it is impossible to determine the variation (increasing, decreasing, periodic, etc.) in brightness unless we have a yardstick by which we can measure the variation. Accordingly we select two reference stars of roughly the same brightness. These reference stars are chosen to have a similar brightness to the lensing event, assuming that the stellar objects of a certain brightness level will be similarly affected by the distortions — such as noise, background, peak intensity and other effects discussed in chapter 2. The stars are also selected to be in the same region as the lensing object to minimise differences in distortions.

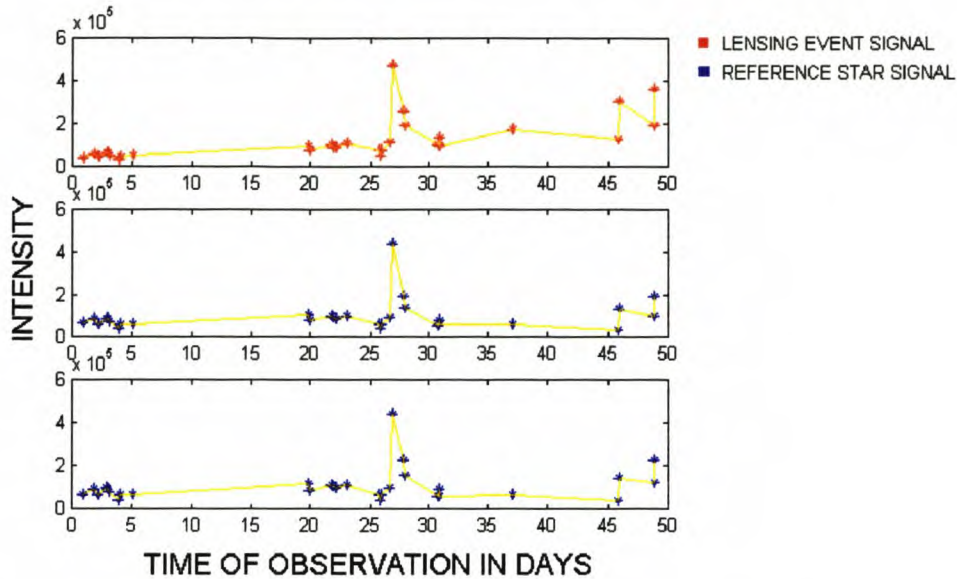


Figure 6.2: The three signals represent the change in the brightness values of three objects over a period of 50 days. The top (red) signal is the data for the lensing event and the bottom two (blue) signals representing the data of the reference stars. The lines (yellow) that connect the data points of each signal is inserted for clarity.

To compare the brightness variations of the three objects, we need to determine the brightness of each of the objects on all our images. Isolating the object and then summing over the area of the object does this. This method of determining the brightness can only be done after subtraction of the background. When we talk about the brightness of the objects, we need to give some idea of the error made during observation, since we do not have a perfect signal, but a signal plus noise (section 2.3.5).

Let us consider a few of the possible errors made when calculating the brightness of the star.

1. Aperture — This is where the greatest error is made. Light from a point source is spread out over an extended area by the atmosphere. The size of this area is governed by the seeing during observation. This makes it difficult to calculate the exact brightness of the star, since it is impossible to determine the absolute area of the star for separation from the background. Even after the brightness values are normalised there are still some apparent fluctuations as seen in the blue graphs of figure 6.13.

2. Observational error — This is determined using the CCD equation (2.6). We find the brightness to be  $I = I \pm 522$ , where 522 is the error calculated from the CCD equation. If we superimpose the respective error bars on a plot of the calculated intensities, we see that errors are smaller than the dots used to plot the values.

In each of the three data sets in figure 6.2 we see a sharp increase in the brightness of one of the data points (outlier), approximately at day 27. These outliers appear in the same position on all three graphs in figure 6.2 with the same apparent increasing tendencies of the surrounding points. Since the behaviour is the same for all three plots, we can assume that it is influenced by some factor of the image from which the data of those three stars are taken. Various reasons can explain this increase, such as an image with a pre-flash during exposure, an error in the subtraction of the background, an error in the isolation of the star, or other influence of outside (extra) brightness-counts. In figure 6.2 the data are represented as a 1-dimensional curve (or signal). The  $x$ -axis represents the time at which the observation was taken (in days) and the  $y$ -axis the determined brightness. In most of the cases the red signal indicates the data for the event, while the blue signals indicates the data for the reference stars.

A visual comparison of the signals shows the following: The data for these three objects are remarkably well behaved, with all three showing similar types of fluctuation. We see that the variations in the seeing conditions are reflected in the fluctuations, with only the one outlier. At first glance it is difficult to detect any definite trends. We do see large variability in the seeing. We need to do a more careful analysis.

## 6.2 Methods of Analysis

### 6.2.1 Data Subtraction

Since it is not possible to determine the absolute brightness from an image, one is forced to consider relative brightness, i.e. the brightness of the target object with respect to its neighbours. A change in relative brightness on successive frames, indicates an absolute change in brightness. In order to measure or detect these changes in relative brightness, the method of signal subtraction can be employed.

If we consider the results obtained after subtracting the signals from each other, the resulting trend is obtained and shown in figure 6.3. The two bottom blue graphs clearly shows

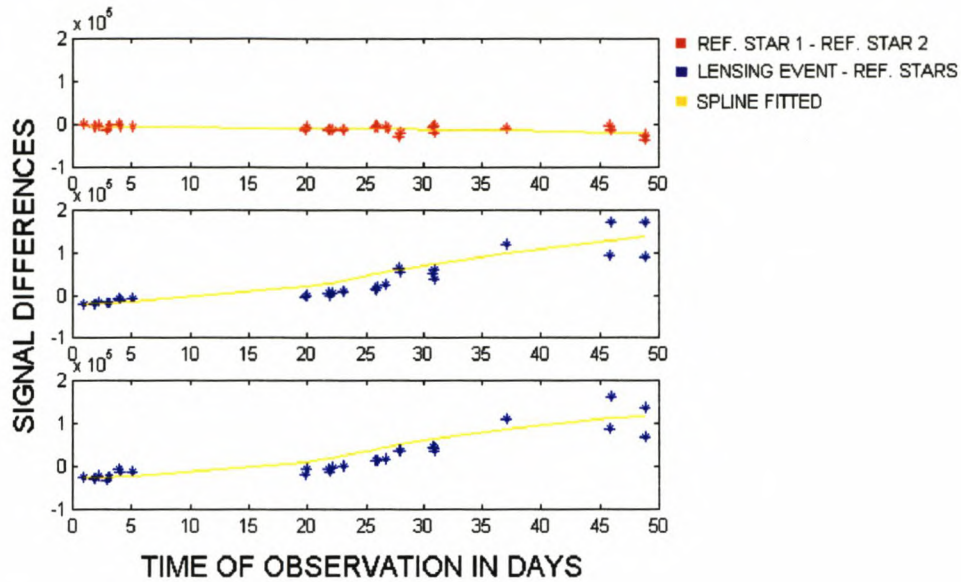


Figure 6.3: The signals are subtracted from each other, with the top graph (red) showing the result after the two reference signals are subtracted. We see no indication of a trend here. The bottom two graphs (blue) show the results after the subtraction of the respective reference signals from the lensing data signal. These two residual graphs do show the increasing tendency of the lensing signal.

an increasing trend as compared with the trends of the two reference signals — the top red graph shows no increase in the reference star trends.

### 6.2.2 Wavelets

When we analyse the data using wavelets — restricting ourselves to the Haar and Daubechies 3 wavelets — we consider the problem at different scales; e.g., the trend is a feature occurring at a larger scale (long-term). Another advantage is that with wavelets, many stars can be investigated, since it is easy to automate and only those objects showing discrepancies can be flagged for further investigation. This will save a lot of unnecessary and tedious user-time trying so sift through heaps of data.

The basic idea is to remove fluctuations on the different scales and to do this until we are left with the long-term trend. Note that this enables us to identify other types of objects such as variable stars. We use the data signals as is — wavelets give us good trend approximation irrespective of the outlying points. We do a multilevel wavelet decomposition of all three signals in the data set, using the Daubechies 3 wavelet. We keep only the lowest level decomposition, where all the fluctuations have been smoothed out leaving only the trend.

To minimize boundary distortions we use the symmetrization signal extension mode that is provided by the MATLAB Wavelet Toolbox. Figure 6.4 shows the trend for each individual object. The trends of the two reference objects are very similar whereas that of the event shows a marked increase.

Since the trend of the reference stars will give us a good indication of a trend behaviour in the image, we use these stars to calculate a trend and subtract it from our data. This normalisation will not clear the trend in the lensing event (which is due to the object) and we can do comparisons between the signals; see figure 6.5.

This method of wavelet analysis has shown itself to be promising in the trend recognition of data, even then only a small sample of data points is available. The very different trend shown by the plot of the lensing event data was echoed in the wavelet plots, leaving no doubts to the increasing tendency of the object.

On the other hand figure 6.6 shows the erratic behaviour of the high-frequency detail coefficients. By combining the low and high frequency coefficients we can reconstruct the original signal.

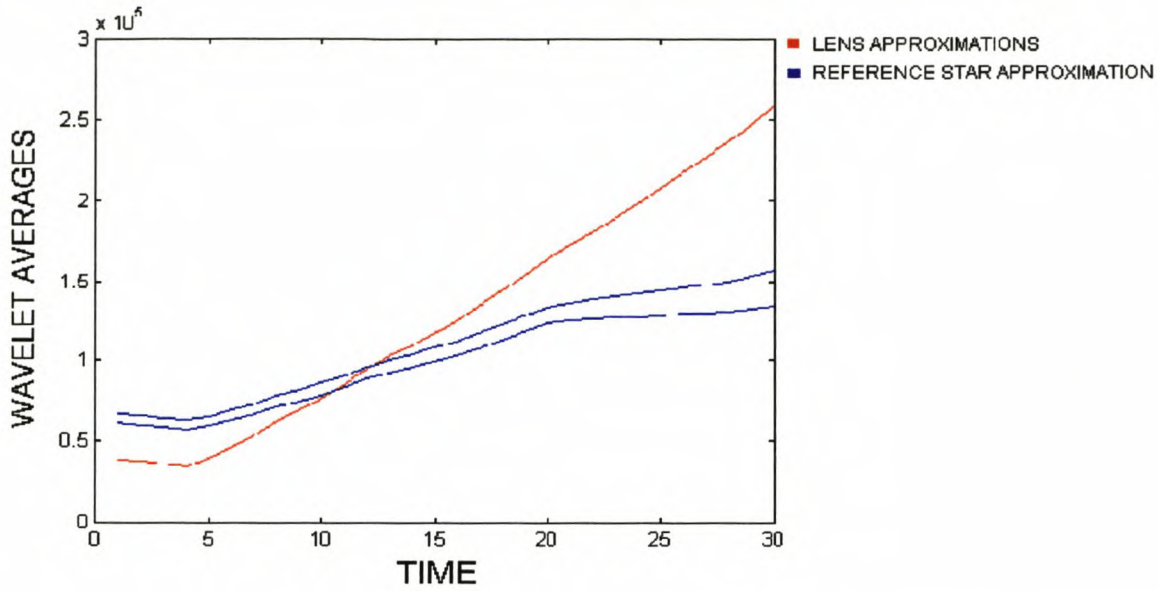


Figure 6.4: Complete set of data points after smoothing with wavelet analysis. The sharply increasing line (red) indicates the trend of the lensing event, while the two curves in close proximity (blue) are the trend of the reference stars.

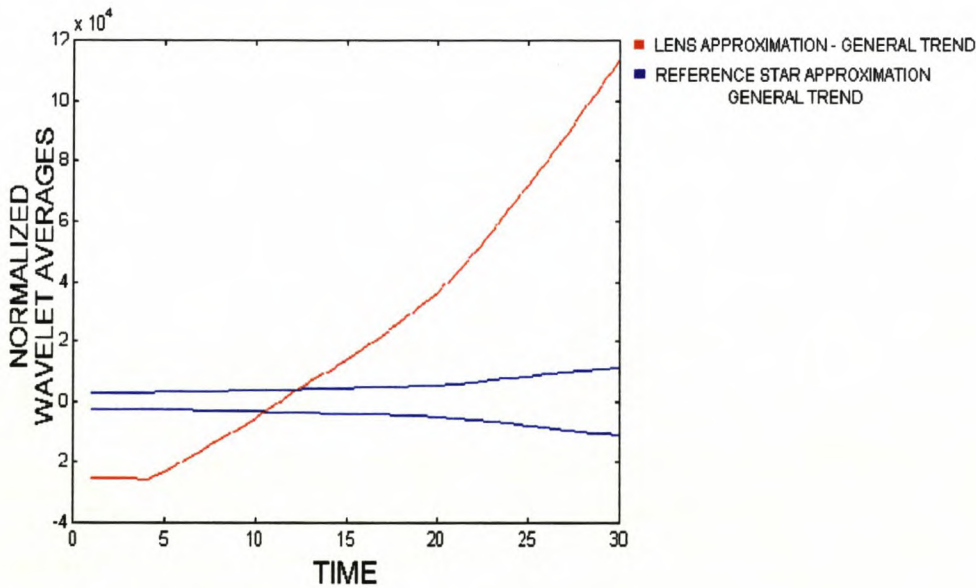


Figure 6.5: If we subtract the averages of the data, as determined using the wavelets, from a general trend, we can clearly see a quantitative increase in the lensing trend. The normalized trends of the reference signals are situated around zero.

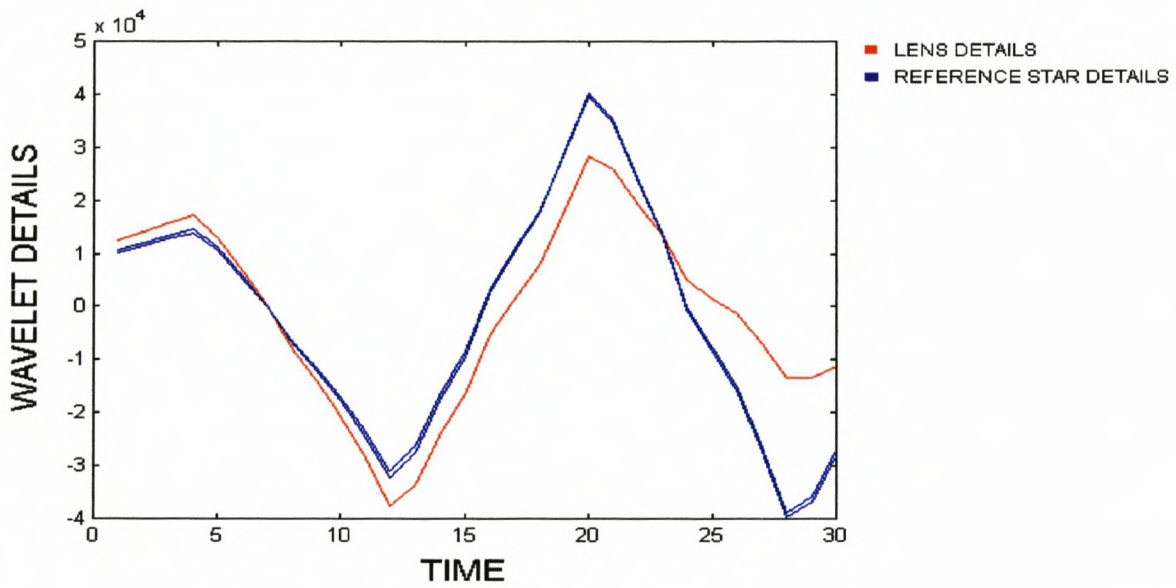


Figure 6.6: Graph showing the behaviour of the detail coefficients. Again we see close correlation for the reference stars and deviations in the detail coefficients of the lensing event, although the behaviour of the detail coefficients of all three signal are similar.

### 6.2.3 General Trend

This method uses much the same approach as wavelets, except that we now use an iterative process (see section 5.3) to calculate a general trend using the reference signals. We normalise the signals by subtracting the general trend from each. The residual curves in figure 6.7 (showing the detrended data) of the two reference signals (blue), which are close to the general trend, show no extraordinary behaviour and are situated closely around zero. On the other hand, the residual curve of the lensing signal (red) shows a very definite increase. It starts below the reference residuals and is still increasing at the end. This correlates closely with the trend determined through wavelet analysis.

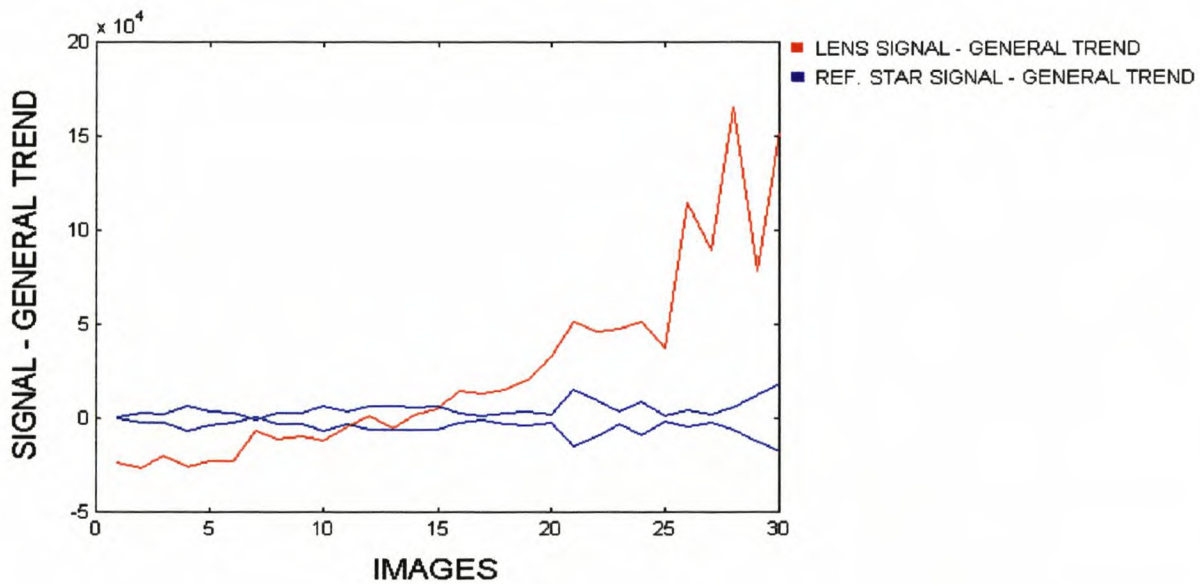


Figure 6.7: The increasing (red) curve shows the residual after the lensing signal was subtracted from the general trend. The two curves (blue) situated around zero are the reference signals subtracted from the general trend.



### 6.3 Finding a Blip

One of the most important features of an automated system is its ability to identify a blip. The detection of a blip is important, because it is an indicator that an object passed between the lens and the source. Our data does not have a blip, so we construct an artificial blip by suppressing the outlier on the signals of the two reference stars, see figure 6.8.

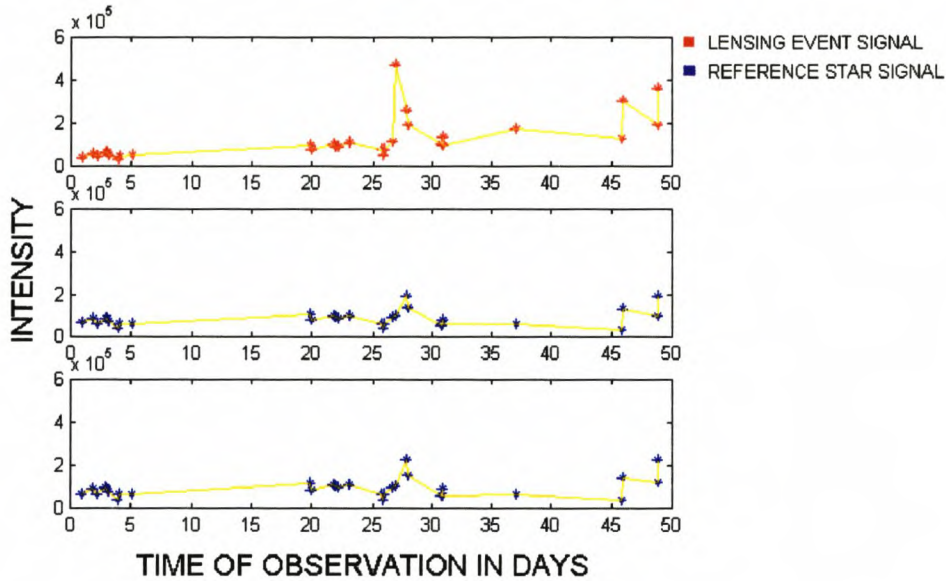


Figure 6.8: Three signals representing the data to analyse, with the top (red) signal showing the lensing data with an artificial blip and the bottom two (blue) signals showing the data for the reference stars without blips.

### 6.3.1 Data Subtraction

By subtracting the signals from each other we are able to see the blip in the data quite clearly, as shown in figure 6.9. The major difficulty is that because of the magnitude of the blip, the trend is not very clear and might even be lost.

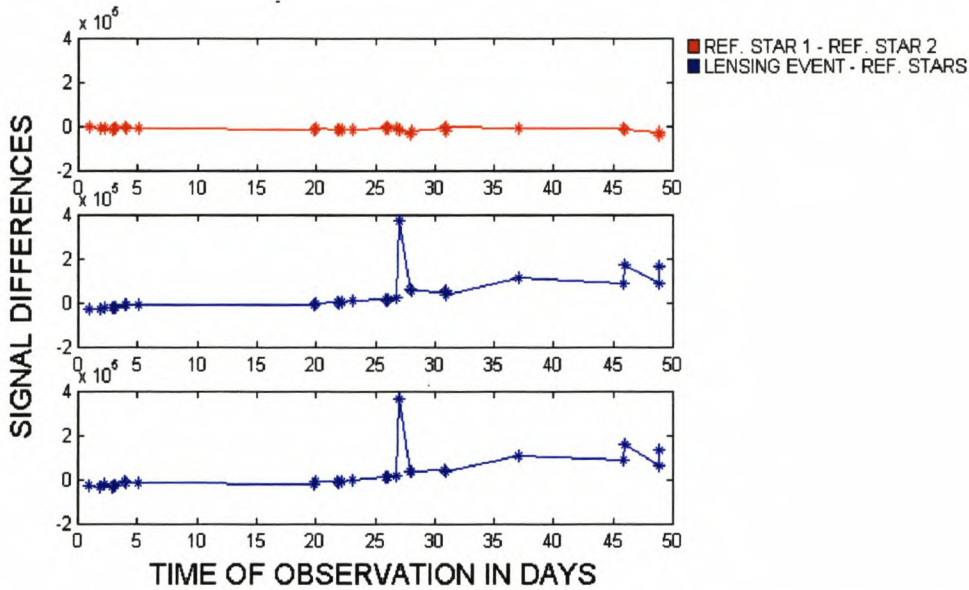


Figure 6.9: The signals with the artificial blip are subtracted from each other. The top graph (red) shows the result after the two signals of the reference stars are subtracted. The behaviour is clearly the same and we see no outliers. The bottom two graphs (blue) show the results after the subtraction of the reference star signals from the lensing data signal respectively. The residual signals clearly show the presence of the blip.

### 6.3.2 Wavelets

Any blip in a data series is expected to be a short-term phenomenon. We apply a small-scale analysis to obtain the information provided by the higher frequencies of the signal (the detail coefficients).

We have successfully identified the trends of the lensing event, but the data does not have any unique outliers. To enable us to study our ability to detect such a blip in the data we use the artificial data set.

To do this kind of analysis, we turn to the Haar wavelet, since it gives the best results for finding local sharp anomalies.

$$w(t) = \begin{cases} 1 & : 0 \leq t < \frac{1}{2} \\ -1 & : \frac{1}{2} \leq t < 1 \\ 0 & : \text{otherwise} . \end{cases} \quad (6.1)$$

We again use multilevel wavelet decomposition with the symmetrization extension mode. We are interested in the local behaviour of the signal and we will focus on the detail coefficients given by the wavelet analysis.

During the first part of the data where there is very little change between the data points (figure 6.2), we see very little fluctuation in the detail as well (figure 6.10). When we reach the part with the blip in the data, we find very noticeable fluctuations occurring in the detail. This happens again during the last few data points; here we see it also in the data for the reference stars (figure 6.12). The fluctuations for the blip are greater than for those of the last points, indicating very specifically where the position of the blip is situated.

This analysis not only allows us to detect the presence of a blip in the data, but also enables us to determine the position of the blip. A comparison with the reference stars shows the presence of the blip very clearly. Figure 6.11 shows the result if the first level details are subtracted from each other.

In figure 6.11, the first graph shows the smoothed graph resulting from the differences between the two standard stars and the bottom two graphs show the respective subtraction of these two graphs from the graph of the lensing event. In using these graphs the differences (and with that the blip) are shown very clearly. The differences towards the end of the series also indicate some anomaly in the data, but the magnitude of the differences caused by the blip is larger. It is impossible to automate the determination of whether these fluctuations actually indicate an anomaly or not. Their distance from the mean trend of the data can

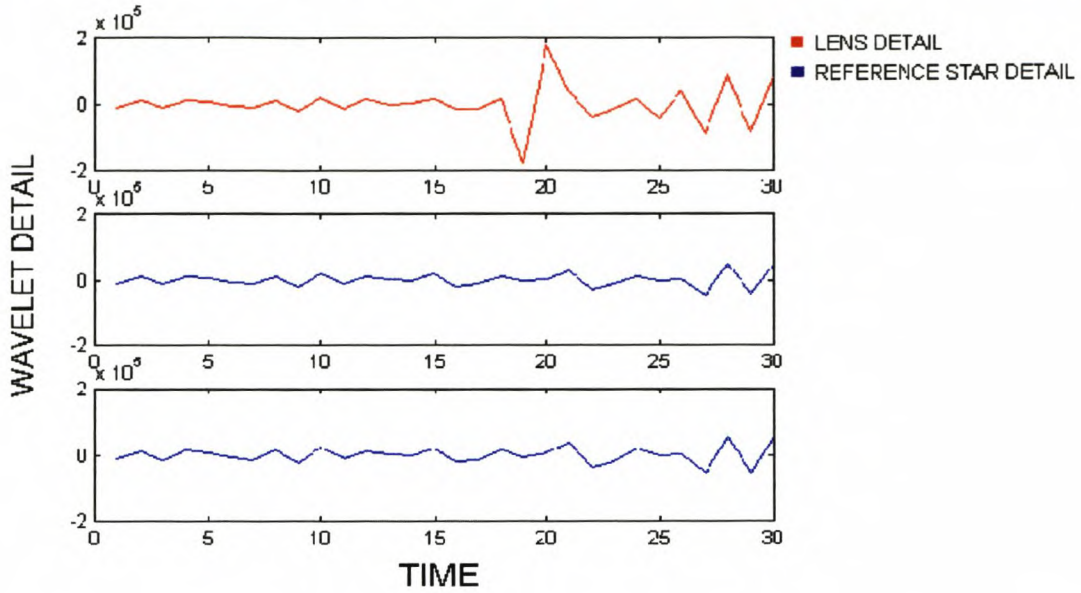


Figure 6.10: Decomposition and detail of the lensing data using the wavelet toolbox graphics display. The top (red) graph showing the detail coefficients for the lensing data and the bottom two graphs (blue) the detail coefficients for the reference data.

however indicate the amount of importance attached to each of the fluctuations.

If we compare the wavelet detail graph of the lensing event (figure 6.12) with the graph produced by the subtraction of the lensing data points we see that they have similar shapes. It is quite clear in the part of the two graphs where the blip is located, showing that both methods give similar results.

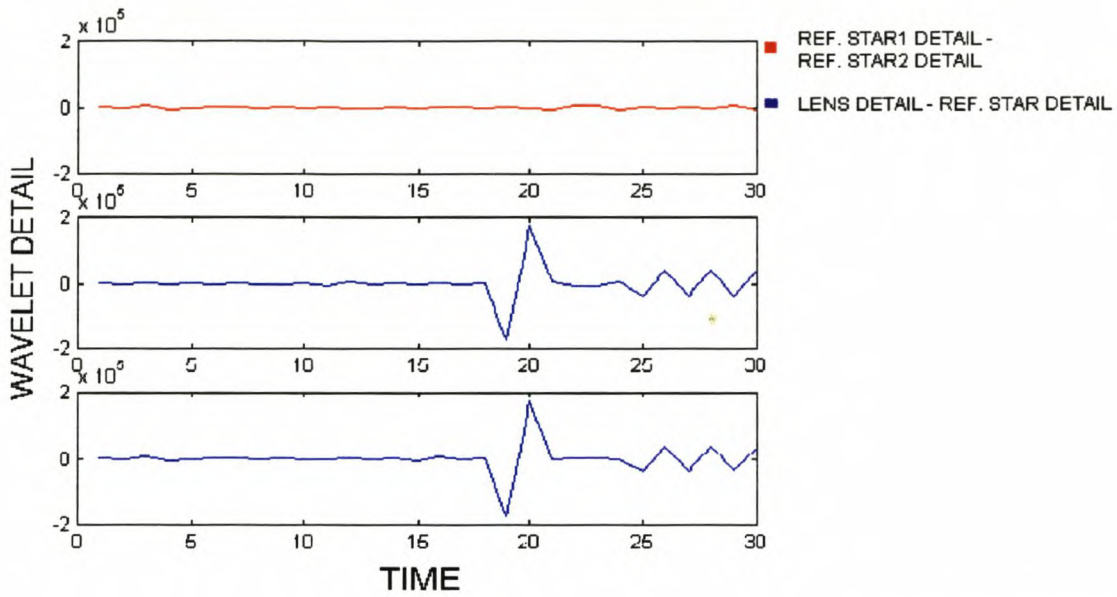


Figure 6.11: The top (red) graph shows the residual after the subtraction of the detail coefficients of the two reference signals. The bottom two graphs (blue) show the residual after subtracting the respective reference detail coefficients from the lensing detail coefficients.

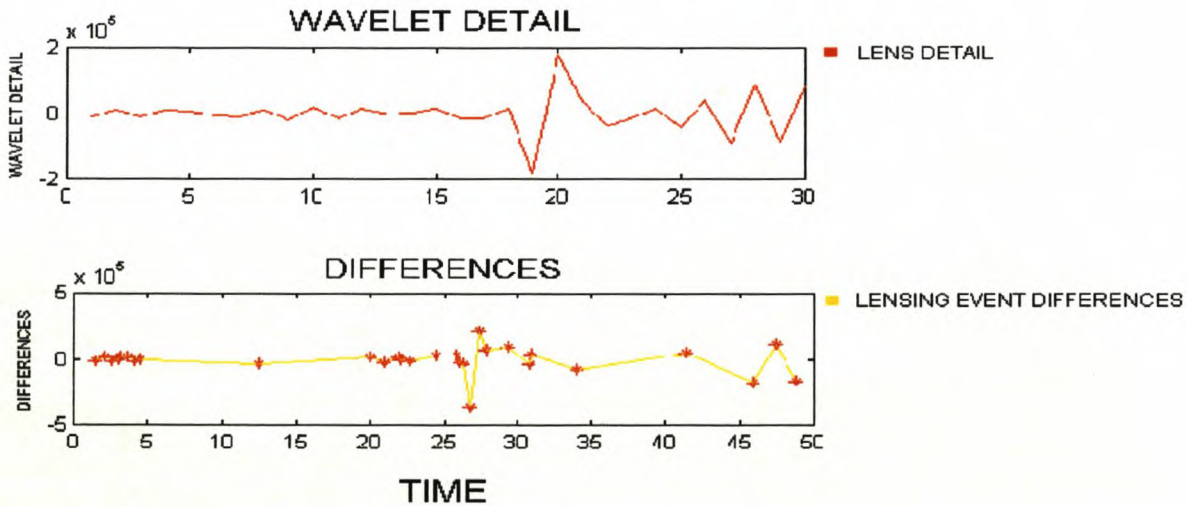


Figure 6.12: The top (red) graph shows the wavelet detail of the data containing the artificial blip. The bottom (yellow) graph shows the differences after the data points of the same data have been subtracted.

### 6.3.3 General Trend

When applying the general trend subtraction technique to the blip data we see the same trend as figure 6.7. We also find a spike superimposed on the signal of the data that clearly indicates the position of the blip (figure 6.13).

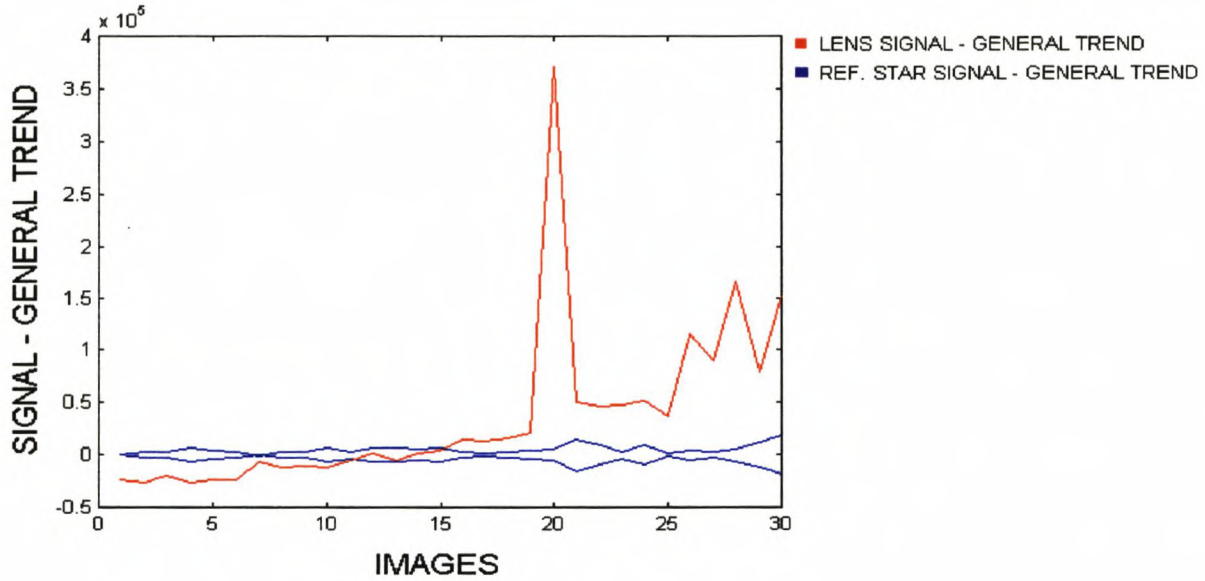


Figure 6.13: Using the data with the artificial blip. The increasing (red) curve shows the residual after the lensing signal was subtracted from the general trend. The two curves situated around zero (blue) are the reference signals subtracted from the general trend.

## 6.4 Locally Weighted Regression (LOESS)

During application of the LOESS technique we need to specify two free parameters, namely the order of the polynomial which is used for local smoothing of the data and the smoothing bandwidth [Koen 1996].

First and second order polynomials are recommended [Cleveland et. al. 1988] and experimentation has shown the locally linear smoothers to be adequate. The level of detail required of the estimated variance function dictates the smoothing bandwidth.

This was the last method applied to the data containing the artificial blip. The data sets were fitted independently and in all three cases we see a good fit. Although we are able to get these fits with the minimum experimentation, this is a method that will be most useful when the optimisation of the fits is automated. We have the option of fitting the data using linear or quadratic polynomials. Since our data do not show a large scatter, a linear polynomial can be used to fit the data. For the lensing data fit we specified the smoothing bandwidth  $f = 0.3$ , since we wanted to smooth the curve, but keep it close to the data points to indicate the blip. For the two reference stars  $f = 0.9$ , since we know that the reference data will fit close to a straight line and does not have any blips. We obtained smooth fits to the data, but still have a clear indication of the position of the blip, as shown in figure 6.14. There is also a very good correlation between the two polynomials fitted through the two reference data sets, shown in figures 6.15 and 6.16.

The value for  $f$  was determined experimentally since we already knew the behaviour of the data. When the method is automated it would be advisable to optimise the determination of  $f$  and to investigate the differences between the values. This is a very strong (but very sensitive) method and it would be well advised to apply this method to a data set containing more data points.

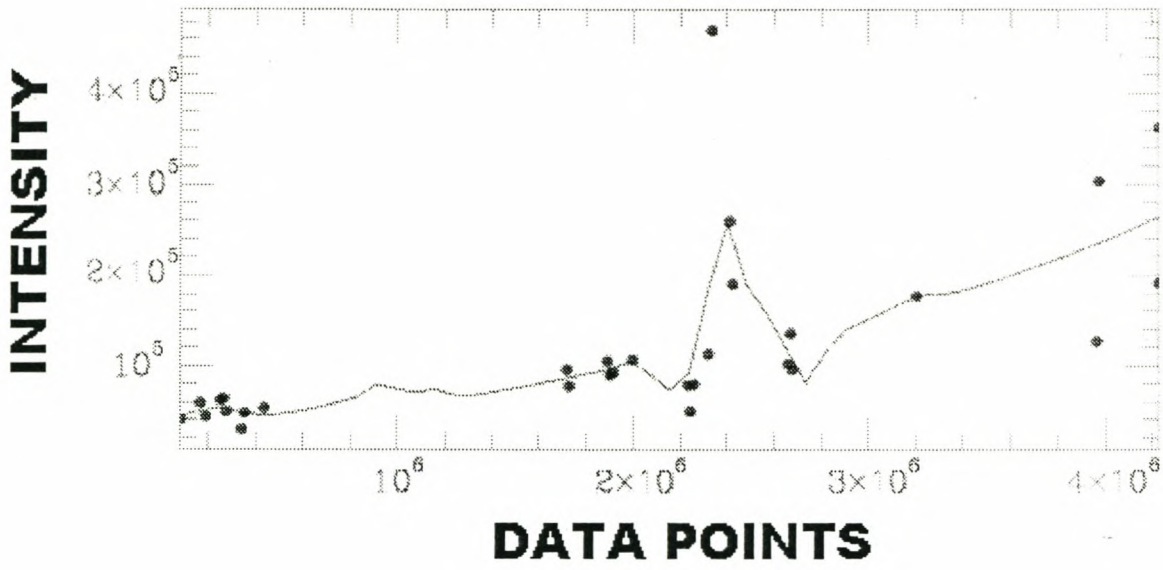


Figure 6.14: LOESS fit through the lensing data containing the artificial blip, using a linear polynomial and  $f = 0.3$ .

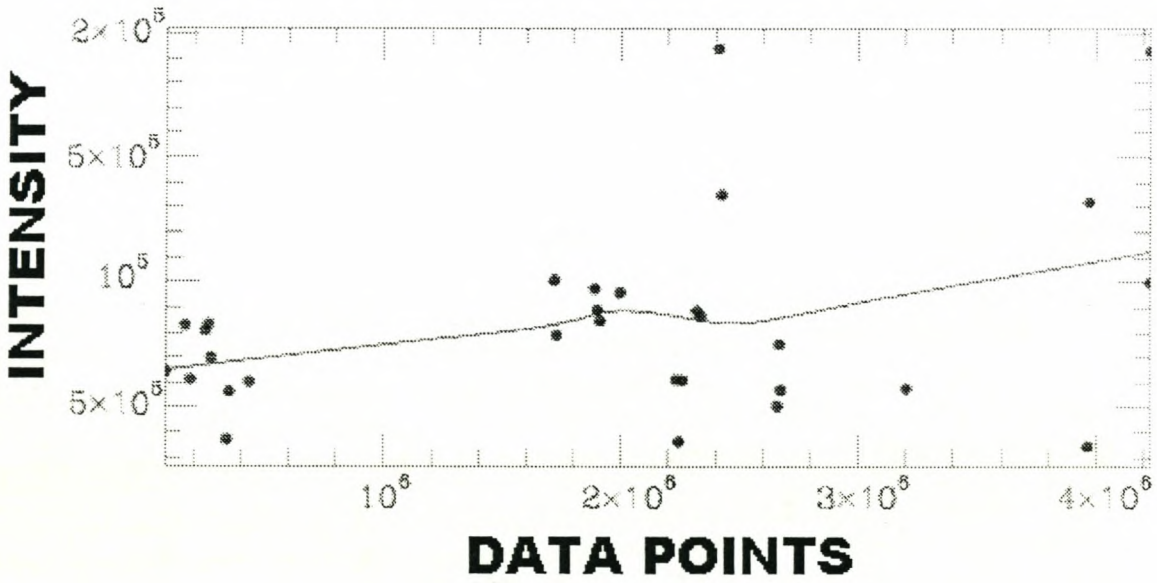


Figure 6.15: LOESS fit through the data of the first reference star, using a linear polynomial and  $f = 0.9$ .



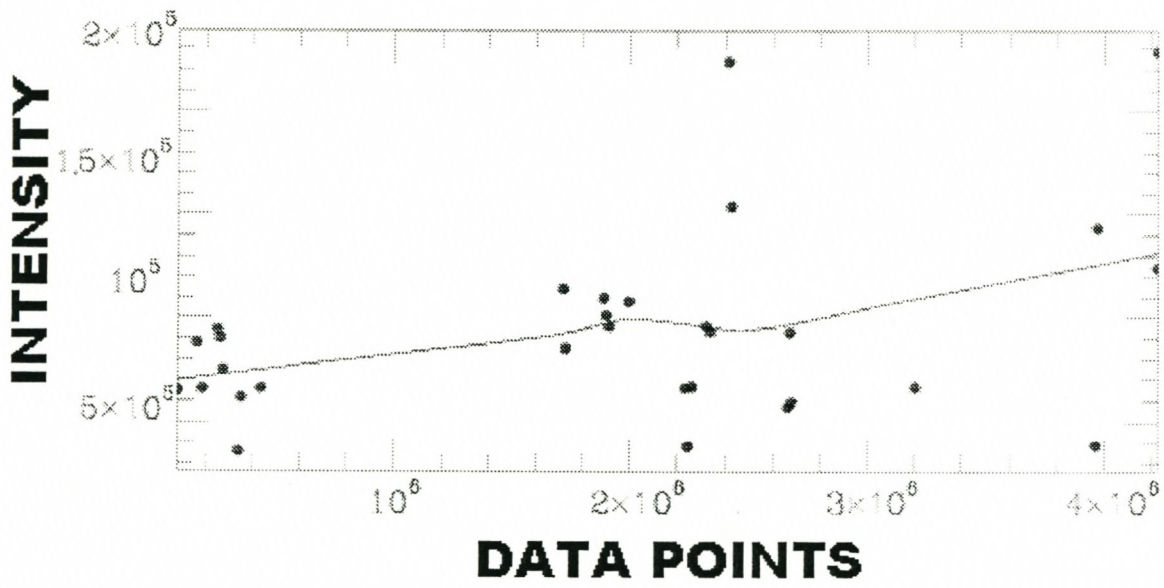


Figure 6.16: LOESS fit through the data of the second reference star, using a linear polynomial and  $f = 0.9$ .

# Chapter 7

## Conclusion

Astronomers are faced with several problems when analysing CCD images containing microlensing events. The most important of these problems are registration, background radiation approximation and the PSF. The analyses of the brightness variations depend on a very accurate determination of the brightness of a stellar object. Even then it is still necessary to normalise the values and to use comparison with nearby stars to get a complete picture of the behaviour of the object.

The aim of this thesis is to suggest new methods for the study of gravitational microlensing events. These methods are aimed at the automation of the detection and analysis of these events.

Instead of using the image subtraction method developed by [Alard 1997] we opted for a direct comparison of the relative brightness values. This approach has several advantages in that it is relatively easy to calculate, it is not computationally intensive, and all information is extracted directly from the image with no assumptions made on the brightness or profile of an object.

Registration is achieved by first correlating two stars using a triangulation procedure and secondly by drawing arcs around these two stars to correlate the rest of the objects on the image. This circle intersection method was thoroughly tested and compared with the existing triangulation method and was proven to be faster as well as more easily adaptable to different subtleties — such as mirror images and misidentification — associated with registration.

Modelling of the influence of the background of an image is done quite accurately using the watershedding algorithm. The advantages of using the watershedding algorithm are

that we can easily identify a range of background pixels that is spread over the whole of the image and we are no longer dependent on isolated stars or sparsely populated stellar images. This is done along with the isolation of the object on the stellar image, which is achieved through the application of the algorithm. However we are unable to make a definite quantitative comparison between the watershedding algorithm and existing techniques — such as taking an annulus around an object — since more tests are needed for a firm conclusion.

Wavelet analysis is an easily automated method for finding both the trend of an object as well as any erratic behaviour such as a blip. This includes the classification of the trend (increasing) and the position of the blip (day 23–30). This method can also be applied to the detection and classification of other objects such as variable stars.

Locally weighted regression showed similar results with the smoothing of the trend while still indicating the presence and position of the blip.

When comparing the results of the different methods used for the analysis of the data, we see very similar results. Again it is very difficult to make direct comparisons between the different methods, since we are unable to perform detailed tests on the more subtle variations that might occur in images taken of different stellar fields. Unfortunately our data set is restricted to the same images for both the training and testing data sets. All we can conclude is that the methods of wavelets analysis and LOESS promise good results, but there is still some development and extensive testing needed.

Future investigation will include the development and completion of this system, along with the necessary testing of the system over a wide range of data — not necessarily containing microlensing events.

# Bibliography

- [Alard 1997] Alard C. and Lupton. R.H., 1997, A method for optimal image subtraction, *Astron. Astrophys*, p.1–8.
- [Alard 1999] Alard. C., 1999, Image subtraction with non-constant kernel solution, *Astron. Astrophys. Manuscript*.
- [ASP conf. ser. 1992] , 1992, Astronomical CCD observing and reduction techniques, *Astronomical society of the Pacific conference series*, vol 23.
- [Bishop 1998] Bishop C.M., 1998, *Neural networks for pattern recognition*, Oxford University Press, p.136–139.
- [Boas 1966] Boas M.L., 1966, *Mathematical methods in the physical sciences*, Wiley international, p.712–714.
- [Borowski et. al. 1989] Borowski E.J. Borwein J.M., 1989, *Collins dictionary of mathematics*, Harper Collins Publishers.
- [Boyd 1978] Boyd R.W., 1978, The wavelength dependence of seeing, *J. Opt. Soc. Am*, vol 68, nr 7, p.877–883.
- [Cleveland 1979] Cleveland W.S., 1979, Robust locally weighted regression and smoothing scatter plots, *Journal of the American Statistical Association*, vol. 74, no. 368, p. 829–836.
- [Cleveland et. al. 1988] Cleveland W.S. et.al., 1988, Locally weighted regression: An approach to regression analysis by local fitting, *Journal of the American Statistical Association*, vol. 83, no. 403, p. 596–610.

- [Cornwell 1987] Cornwell T.J., 1987, Radio-interferometric imaging of weak objects in conditions of poor stability: The relationship between speckle masking and phase closure methods, *Astron. Astrophys.*, vol 180, p269–274.
- [Da Costa 1992] Da Costa G.S., 1992, Basic photometry techniques, *ASP. conference series*, vol.23, p.90–104.
- [De Boor 1963] De Boor C., 1963, *A practical guide to splines*, Springer-Verlag, p. 235–249.
- [Gonzales et. al. 1993] Gonzales R.C. and Woods. R.E., 1993, *Digital image processing*, Addison-Wesley, p.173–180.
- [Gullixson 1992] Gullixson C.A., 1992, Two-dimensional imagery, *ASP Conference series*, vol 23, p.130–159.
- [Gunn 1995] Gunn J.E., 1995, The Sloan digital sky survey, *American Astronomical Society*, vol 186.
- [Herbst 1999] Fornberg B. and Herbst B., *Modeling in applied mathematics*, unpublished.
- [Hopkins 1980] Hopkins J., 1980, *Glossary of astronomy and astrophysics*, University of Chicago Press.
- [Howell 1989] Howell S.B., 1989, Two-dimensional aperture photometry: Signal-to-noise ration of point-source observations and optimal data-extraction techniques, *Publications of the Astronomical Society of the Pacific*, vol.101, p.616–622.
- [Jain 1989] Jain A.K., 1989, *Fundamentals of digital image processing*, Prentice Hall, p.276–292.
- [Koen 1996] Koen C., 1996, The analysis of indexed astronomical time series, *Mon. Not. R. Astron. Soc.*, vol 283, p471–537.
- [Marcy et. al. 1998] Marcy G.W. and Butler R.P., 1998, Detection of extrasolar giant planets, *Annual. Rev. Astron. and Astrophys.*, vol 36, p.57.
- [Masson 1993] Masson C.R., 1993, *Seeing*, Very high Angular Resolution Images, p.1–10.
- [Mateo et. al. 1993] Mateo M.L. et. al., 1993, *JUSTDoIT!! A DoPHOT USER'S MANUAL*.
- [Misiti et. al. 1996] Misiti M. et. al., 1996, *MATLAB: Wavelet toolbox*.

- [NASA 1990] NASA, 1990, *Flexible image transport system (FITS)*, NASA Science Data Systems Standards Office.
- [Paczynski 1996] Paczynski. B., 1996, Gravitational microlensing in the local group, *Annu. Rev. Astron. Astrophys.*, p. 419–459.
- [Rice 1988] Rice J.A., 1988, *Mathematical statistics and data analysis*, Duxbury Press, p.223–234.
- [Ridpath 1997] Ridpath I., 1997, *Dictionary of astronomy*, Oxford University Press.
- [Sackett 1999] Sackett P.D., 1999, *Searching for unseen planets via occultation and microlensing*, Planets Outside the Solar System: Theory and Observations, p189.
- [Schechter et. al. 1993] Schechter P.L. et.al., 1993, DoPHOT, A CCD photometry program: Description and tests, *Publications of the astronomical society of the pacific*, p. 1342–1353.
- [Shu 1982] Shu F.H., 1982, *The physical universe, an introduction to astronomy*, University Science Books.
- [Smith 1996] Smith C.C.J. et.al., 1996, *Boundingbox: A simple human gesture classification system*, De Beers Consolidated Mines Ltd. and the University of Pretoria, p.50–54.
- [Stetson et. al. 1986] Stetson R.B. et.al., 1986, Future development of the DAOPHOT crowded-field photometry package, *ASP Conference Series*, p. 289–304.
- [Strang 1997] Strang G. and Nhuyen T., 1997, *Wavelets and filter banks*, Wellesley-Cambridge Press, p.1–35.
- [Vincent 1991] Vincent L. and Soille P., 1991, Watersheds in digital space: An efficient algorithm based on immersion simulations, *IEEE Transactions on Pattern Analysis and Machine Intelligence*, vol 13, no 16, p.583–598.
- [Walker 1981] Walker A.R., 1981, The airglow spectrum from 5 500–7 000 angstroms, *SAAO circulars*, nr 6, p.101.
- [Young 1974] Young A.T., 1974, Seeing: Its cause and cure, *The Astrophysical Journal*, vol 189, p.587–604.

# Appendix A: Data Images

We now describe the data images that were used during our investigations in more detail. To do this we must first give an explanation of the format of the images.

## FITS-standard used for image format

FITS is an abbreviation of the name Flexible Image Transport System. The flexible image transport system's development was necessitated by the need for a standard format for the transferring of astronomical data from one installation to another.

The FITS files are self-documenting image files that are divided into two primary parts.

The first part is the ASCII<sup>1</sup> headers and the second is the binary arrays that contain the data of the images. The scope of this project will be restricted to the basic FITS files, since there was no need for us to investigate the more complicated format options.

In the basic FITS format the structure consists only of a primary header and a primary data block containing a single array.

## Quick overview of the overall structure of FITS files

Elements and order of FITS files:

- Primary HDU<sup>2</sup>
- Extensions (optional)
- Special records (optional)

---

<sup>1</sup>ASCII: American Standard Code for Information Interchange. A code used in computing to represent letters, numbers and other standard symbols

<sup>2</sup>Header and Data Unit (HDU) is a data structure consisting of a Header and the data describing the Header.

Each FITS element must consist of an integral number of FITS logical records. The size of each record is specified to be 23 040 bits (or 2 880 8-bit bytes). The primary HDU starts with the first record of the FITS file and must be comprised of an integral number of header records that consists of ASCII text. This is immediately followed by an integral number of data records, with the first binary data record following directly after the last header record. This primary header must always be the first component of a FITS data set and need not be followed by primary data. If so, then the data must follow immediately as explained above.

The primary data may be either in Basic FITS array format or random group format. It may happen that the ASCII code of the primary header or the binary data of the primary data block does not fill their respective last records. Then the primary header's record must be filled with blanks and the data array must be filled with zeros-values, with the same data representation as the values in the array.

Both the data of the primary header and the primary binary data block must be saved in one long array.

We will proceed to give short descriptions of the two parts of the FITS file format that was mentioned above, namely the ASCII header and the binary data block.

## Headers

This is the self-documenting ASCII part of the FITS file. (The reader familiar with for example the BMP format will recognise this.) This documentation provides the user with all the necessary information concerning the binary image that follows.

Syntax: Each header card image must consist of a keyword, an optional value and an optional comment. The few keywords mentioned here are the principal mandatory keywords. Most of these principal keywords must appear first in the header (and in the order as indicated by the numbering below) with only the END keyword appearing last to indicate the end of the ASCII header card. Each header card image is assigned a size of 80 columns and the keywords must occupy the first 1-8 bytes of each header card.

Principal Keywords:

1. SIMPLE: indicates if the file is a standard FITS file (T) or not (F)
2. BITPIX: indicates the format of the number representation
3. NAXIS: number of dimensions of the binary image below



4. NAXISn: dimensions of the image matrix

:

Last is END: end of the header block

The value indicators will follow in bytes 9–10. These columns are reserved for when values are to be assigned to any particular keywords. If a value is present, then column 9 must contain the symbol '=' and column 10 must be blank.

Following this the character strings will start with a single quote in column 11 and end with a single closing quote between columns 20–80.

Logical variables must be a T or an F in column 30. (T indicating that the file is a true standard FITS format file.)

Integer values must be right justified in columns 11–30, with the imaginary part of complex numbers right justified in columns 31–50.

Floating-point numbers are also right justified in columns 11–30 and the decimal point must appear.

Comments can occupy the space from bytes 11–80. Thus the remainder of bytes in the card image may be filled with comments. With the separation between the value and the comment indicated by a slash (/) and a space.

## Data Records

This is the binary second part of the basic FITS file that contains the image. This part must immediately follow the last block of the primary header. The data values must be stored as a bit-stream, with no embedded blank spaces. The first value is stored in the first position of the first array record. The first value of all subsequent records will immediately follow the last value of the previous record. The remainder of the last data record, following the last element of the array must be filled with zero values as described previously. The dimensions of the image is as specified by the header.

Since we have now only provided a very short summary of the format of the FITS files, the reader might be interested in investigating this for himself. To this end we provide a short manual, but the reader may also familiarise himself with the documentation that is readily available on the internet<sup>3</sup>.

---

<sup>3</sup>For more information: [fits@nssdca.gsfc.nasa.gov](mailto:fits@nssdca.gsfc.nasa.gov)

## Appendix B: Seeing

The angular resolution<sup>4</sup> of an astronomical telescope is often limited primarily by atmospheric turbulence [Boyd 1978], and this resolution limitation is conventionally referred to as atmospheric seeing.

The optical path fluctuations are dominated by tropospheric density variations [Masson 1993]. At optical wavelengths ( $\lambda \sim 500nm$ ), where most telescopes are large filled apertures, diffraction effects during long exposures give rise to blurred stellar objects. For a circular aperture, the blurring produced by diffraction limits the angular resolution to an amount given by  $\Theta = \frac{1.22\lambda}{d_e}$ , where  $d_e$  (typically  $\sim 10cm$ ) is an effective telescope diameter of an image [Shu 1982].

The turbulent flow can be described statistically for turbulent eddies of scale size  $l \ll L$ , where  $L$  is called the outer scale of the turbulent flow where turbulence is injected, for example by flow past an obstacle. The turbulence is damped out for eddies of size smaller than  $l_0$ , which is the inner scale of the turbulence. For turbulent eddies within the interval  $l_0 \ll l \ll L$ , the turbulence is isotropic (independent of the direction along which the fluctuations are measured), and its intensity depend only on the single parameter  $\epsilon$ , which is the turbulent-energy dissipation rate per unit mass.

Since it is mainly the turbulent elements comparable to or smaller than the telescope aperture that affect image structure, the Kolomogorov law is valid for computing atmospheric seeing effects [Young 1974]. In order to describe the turbulent atmosphere in a statistical sense, it is useful to define the structure function for velocity fluctuations as  $D_v(\mathbf{r}) = \langle [v(\mathbf{R}) - v(\mathbf{R} + \mathbf{r})]^2 \rangle$ , where  $v$  is any component of the velocity vector  $\mathbf{v}$  (the velocity at which to atmosphere moves past the telescope), and  $D_v(\mathbf{r})$  is independent of  $\mathbf{R}$  for isotropic turbulence and  $\langle . \rangle$  denotes the mean. The intensity of the turbulence de-

---

<sup>4</sup>Angular resolution is the ability to distinguish fine details in the image by attempting to bring the light from the source to an accurate focus.

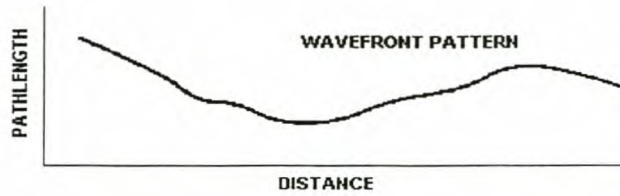


Figure 1: Illustration of the wavefront distortions of the light as it passes through the atmosphere.

depends only on the parameter  $\epsilon$ , and the velocity difference for points separated by the distance  $\mathbf{r}$  will be due mainly to eddies of size comparable to  $\mathbf{r}$ .  $D_v(\mathbf{r})$  can depend only on  $\epsilon$  and  $\mathbf{r}$ , and the only combination of these having the dimensions of  $D_v(\mathbf{r})$  is  $(\epsilon r)^{\frac{2}{3}}$ . Thus  $D_v(\mathbf{r}) = C(\epsilon r)^{\frac{2}{3}}$ , where  $C$  is the velocity structure coefficient. This is the 'two-thirds law' of Kolomogorov and Obukhov [Boyd 1978].

More relevant to the calculation of imaging properties are the statistics of the fluctuations in refractive index. These are assumed to be due to fluctuations in the air temperature, because fluctuations in pressure are assumed to achieve mechanical equilibrium very quickly. Temperature fluctuations are treated by assuming that local temperature is a property that is carried along by the turbulent flow, and temperature is thus known as a conservative passive addition to the flow. Temperature fluctuations are thus broken down by the turbulent flow to progressively smaller scales until they reach a size comparable to  $l_0$  at which point molecular-diffusion processes even out the fluctuations. The rate at which temperature fluctuations are generated must equal the rate at which they are dissipated.

Thus, after traversing the atmosphere, the wave front will be randomly distorted.

A simple description of a wavefront distorted by the atmosphere is shown in figure A1. A distant source produces plane wave fronts at the top of the atmosphere, which are then wrinkled by the turbulent path fluctuations in the atmosphere.

This atmospheric seeing can generally be assumed to have a Gaussian point spread function of variable width.

When we have good seeing, the atmosphere is less turbulent. This means that the localised area in which the point source is represented as a stellar object on the image is much more concentrated. Consequently a high signal to noise ratio is reached during a shorter exposure time.

## Appendix C: Poisson Statistics

Throughout the discussions of the noise on the image, it is assumed that the noise behaviour of bright stars can be described using Poisson statistics. To clarify this we will insert a short example.

The source (star) does not emit the photons in one continuous burst, but rather as photon clumps.

Since this can be compared with the emission of alpha particles from radioactive sources, let's take a quick look at the basic model developed for these alpha particle emissions.

What is noteworthy about the emission of alpha particles is that the number of particles emitted per unit time is constant, but fluctuates in a seemingly random fashion.

To assume the Poisson distribution as a model for random counts in time, the following assumptions must be made:

1. The underlying rate at which the emissions occur must be constant in time.
2. Events in disjoint intervals of time occur independently.
3. There are no multiple events.

We use the same model for the counting of photons by the CCD: We are working with stars that have time dependent intensities. Thus their intensities can change with time. We can therefore assume that (just as in the case of the radioactive source) photon-statistics are applicable in this situation, because

$$\frac{\text{time interval } (dt) \text{ between two photon emissions}}{\text{period of change}} \ll 1 \quad (1)$$

There are a number of ways to test the plausibility of using the Poisson model:

1. Test whether the time intervals between events follow an exponential distribution. If we note the time intervals during the experiment and we look at their distribution we must find that it is exponentially distributed.

2. Test whether the intervals are independent of each other.
3. Test if the counts in a time interval of a specified length follow a Poisson distribution (figure C1).

For our model we have the probability for the emission of one photon during the small time interval  $dt$  to be  $\mu dt$  with  $\mu$  a constant [Boas 1966].

Say we want the probability  $P_n(t)$  of observing exactly  $n$  counts during a time interval  $t$ . Thus  $P_n(t + \Delta t)$  is the probability of observing  $n$  counts in the time interval  $(t + \Delta t)$ .

For  $n < 0$  the  $P_n(t + \Delta t)$  is the sum of the probabilities of two mutually exclusive events,

$$P_n(t + \Delta t) = P_n(t)P_0(\Delta t) + P_{n-1}(t)P_1(\Delta t). \quad (2)$$

(Meaning  $n$  photons during time interval  $t$  and none during  $\Delta t$  and  $(n - 1)$  photons during  $t$  and one during  $\Delta t$ )

Since  $P_1(\Delta t)$  is the probability of one photon during  $\Delta t$ :

$$P_1(\Delta t) = \mu \Delta t \quad (3)$$

(where  $\Delta t$  is the small time interval  $dt$ ).

The probability for no photons during  $\Delta t$  is

$$1 - P_1(\Delta t) = 1 - \mu \Delta t. \quad (4)$$

If we substitute this into (C2):

$$P_n(t + \Delta t) = P_n(t)[1 - \mu \Delta t] + P_{n-1}(t)[\mu \Delta t] \quad (5)$$

it follows that

$$\frac{P_n(t + \Delta t) - P_n(t)}{\Delta t} = \mu[P_{n-1}(t) - P_n(t)]. \quad (6)$$

If we now take the limit  $\Delta t \rightarrow 0$ :

$$\frac{dP_n(t)}{dt} = \mu[P_{n-1}(t) - P_n(t)] \quad (7)$$

for  $n = 0$  (no photons during  $t$  or  $\Delta t$ ) we can simplify (C7):

$$\frac{dP_0}{dt} = -\mu P_0(t). \quad (8)$$

The probability for no photons being emitted during  $t = 0$  is  $P_0(0) = 1$

and by integrating (C8) we get:

$$P_0 = e^{-\mu t}. \quad (9)$$

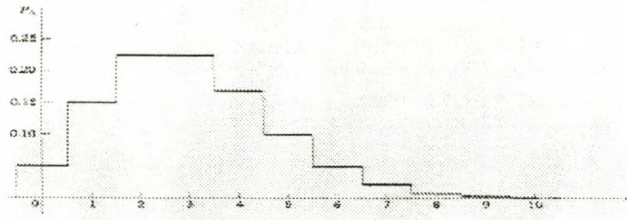


Figure 2: A typical Poisson density distribution function.

Substituting (C9) into (C7) and for  $n = 1$ ; we obtain

$$P_1(t) = \mu t e^{-\mu t} \quad (10)$$

Finally solving

$$\frac{dP_n(t)}{dt} = \mu P_{n-1}(t) - \mu P_n(t) \quad (11)$$

for  $P_2, P_3, \dots, P_n$  it follows that

$$P_n(t) = \frac{\mu^n t^n}{n!} e^{-\mu t}. \quad (12)$$

The value  $t = 1$  gives the probability of  $n$  counts per unit time; i.e.,

$$P_n = \frac{\mu^n}{n!} e^{-\mu} \quad (13)$$

where  $\mu$  is the average number of counts per unit time.